FACULTY OF HEALTH SCIENCES
DIVISION OF BIOMEDICAL ENGINEERING

3D approximation of scapula bone shape from 2D X-ray images using landmark-constrained statistical shape model fitting.

Author:

Wasswa William

(WLLWAS003)

Supervisor:

Dr Tinashe Mutsvangwa

Co-Supervisor:

Professor Tania Douglas

Submitted to the Department of Human Biology at the University of Cape Town in partial fulfilment of the academic requirements for the degree of
MSc (Med) in Biomedical Engineering by
coursework and dissertation.

July 2016

DECLARATON

I, Wasswa William, hereby declare that the work on which this dissertation is based is my original work (except where acknowledgements indicate otherwise) and that neither the whole work or any part of it has been, is being, or is to be submitted for another degree in this or any other university.

I empower the university to reproduce for the purpose of research either the whole or any portion of the contents in any manner whatsoever.

Signed: Signed by candidate Signature Removed

Date: 14/07/2016

ABSTRACT

Two-dimensional X-ray imaging is the dominant imaging modality in low-resource countries despite the existence of three-dimensional (3D) imaging modalities. This is because fewer hospitals in low-resource countries can afford the 3D imaging systems as their acquisition and operation costs are higher. However, 3D images are desirable in a range of clinical applications, for example surgical planning. The aim of this research was to develop a tool for 3D approximation of scapula bone from 2D X-ray images using landmark-constrained statistical shape model fitting.

First, X-ray stereophotogrammetry was used to reconstruct the 3D coordinates of points located on 2D X-ray images of the scapula, acquired from two perspectives. A suitable calibration frame was used to map the image coordinates to their corresponding 3D real-world coordinates. The 3D point localization yielded average errors of (0.14, 0.07, 0.04) mm in the **X**, **Y** and **Z** coordinates respectively, and an absolute reconstruction error of 0.19 mm.

The second phase assessed the reproducibility of the scapula landmarks reported by Ohl et al. (2010) and Borotikar et al. (2015). Only three (the inferior angle, acromion and the coracoid process) of the eight reproducible landmarks considered were selected as these were identifiable from the two different perspectives required for X-ray stereophotogrammetry in this project.

For the last phase, an approximation of a scapula was produced with the aid of a statistical shape model (SSM) built from a training dataset of 84 CT scapulae. This involved constraining an SSM to the 3D reconstructed coordinates of the selected reproducible landmarks from 2D X-ray images. Comparison of the approximate model with a CT-derived ground truth 3D segmented volume resulted in surface-to-surface average distances of 4.28 mm and 3.20 mm, using *three* and *sixteen* landmarks respectively. Hence, increasing the number of landmarks produces a posterior model that makes better predictions of patient-specific reconstructions. An average Euclidean distance of 1.35 mm was obtained between the three selected landmarks on the approximation and the corresponding landmarks on the CT image. Conversely, a Euclidean distance of 5.99 mm was obtained between the three selected landmarks on the original SSM and corresponding landmarks on the CT image. The Euclidean distances confirm that a posterior model moves closer to the CT image, hence it reduces the search space for a more exact patient-specific 3D reconstruction by other fitting algorithms.

ACKNOWLEDGEMENTS

I would like to express my sincere gratitude and appreciation to the people who have supported my research in various ways.

Dr T. Mutsvangwa (Division of Biomedical Engineering) for the research supervision, guidance, support and availability whenever I was in need of assistance.

Prof. T. Douglas (Division of Biomedical Engineering) for the research supervision, guidance, support and provision of resources for the project.

Dr K. De Jager (Division of Biomedical Engineering) for guidance and consultation throughout my research.

Dr S. Sivarasu (Division of Biomedical Engineering) for consultation on the potential applications for my research in prosthesis design and shoulder rehabilitation.

Mr S. Steiner (Division of Biomedical Engineering) for consultation on the working principles of the Lodox Statscan system and 2D X-ray imaging.

Ms K. Nafeesa (Division of Biomedical Engineering) for scanning the cadaveric shoulder using the Lodox Statscan system to obtain the 2D scapula images as well as for selecting the reproducible landmarks from the scapula radiographic images and 3D models.

Ms C. Chimhundu (Division of Biomedical Engineering) for consultation on the X-ray stereophotogrammetry technique as well as guidance on the use of the calibration frame used for X-ray stereophotogrammetry.

Mr C. Harris (Division of Biomedical Engineering) for drilling into the 3D printed scapula and inserting the radio-opaque steel bearings on the selected landmarks.

Dr R. Dendere (Division of Biomedical Engineering) for consultation throughout my research.

Mr D. Roopam (Division of Biomedical Engineering) for consultation on 3D printing.

Lastly, I thank my family members: my parents, **Mr S. William** and **Mrs S. Joyce** for their support and prayers, my sisters **Ms N. Joyce** and **Ms N. Phiona** for their motivation, my brothers **Mr K. Brian**, **Mr K. Robert** and **Mr S. Moses** for continuous support and finally, my beloved wife **Mrs A. Sandrah** for continuous motivation, prayers and support.

TABLE OF CONTENTS

LIST OF FIGURES

LIST OF TABLES

ABBREVIATIONS

1D	One dimensional
2D	Two dimensional
3D	Three dimensional
AAM	Active Appearance Models
ANOVA	Analysis of Variance
AP	Anteroposterior
ASM	Active Shape Models
AWT	Abstract Window Toolkit
CI	Confidence Interval
CT	Computed Tomography
DLT	Direct Linear Transform
DVS	Digital Viewing System
EOS	A digital low-dose bi-plane X-ray imaging system
GPU	Graphics Processing Unit
GUI	Graphical User Interface
HREC	Human Research Ethics Committee
ICC	Intraclass Correlation Coefficient
ILD	Inter-landmark Distance
JVM	Java Virtual Machine
LPS	Left, Posterior, Superior coordinate system
LSSR	Linear Slot Scanning Radiography
MATLAB	Matrix Laboratory
MRI	Magnetic Resonance Imaging

POSIT	Pose from Orthography and Scaling with Iterations
RMS	Root-Mean Square
RSA	Roentgen Stereophotogrammetry Analysis
SD	Standard Deviation
SSD	Sum of Squared Differences
SSM	Statistical Shape Model
SVD	Singular Value Decomposition

1 INTRODUCTION

1.1 Background

After the discovery of X-rays in 1895 by Conrad Roentgen, the first X-ray being of his wife's hand, the medical community quickly recognized the importance of the discovery for clinical use (Peh, 1995). X-ray imaging is the oldest and most common form of medical imaging and provides a quick and non-invasive approach to medical diagnosis (Chen et al., 2012).

Trends in medical imaging show that there is a general shift from 2D to 3D imaging (Sakas, 2002). Three-dimensional imaging provides 3D volume patient data that can be used for guiding intervention, controlling therapy and monitoring the course of illness. However, 2D X-ray imaging modalities are still the dominant modalities in low resource countries, despite the availability of 3D imaging modalities like magnetic resonance imaging (MRI) and computed tomography (CT). This is because fewer hospitals in these countries can afford to buy CT or MRI scanners as their acquisition and operation costs are higher than for 2D imaging (Baka et al., 2011). 3D imaging modalities, however, are desirable in clinical interventions as they provide a 3D view of the region of interest to the surgeon or clinician and are useful in pre-operative, intra-operative and post-operative interventions. Furthermore, 3D images may be easier to interpret for clinicians and untrained researchers, and they can be used for increasing diagnostic accuracy (Heinonen et al., 1998).

Patient-specific 2D-3D reconstruction makes it possible to reconstruct 3D images from 2D X-ray images. However, there is still low adaption to patient-specific 2D-3D bone reconstructions due to the complexity of the methods required to produce clinically useful 3D reconstructions. 2D to 3D image reconstruction is a method of registering a patient's 2D image to a 3D volume or model (Kotsas and Dodd, 2011). Different 2D-3D reconstruction methods have been proposed that utilise statistical shape models (SSMs) to reconstruct patient-specific 3D models from two or more 2D X-ray images (Laporte et al., 2003; Zheng et al., 2009; Yokota et al., 2009, Kurazume et al., 2009). The reported successes in reconstruction of 3D patient-specific models from 2D X-ray images for medical image analysis, along with the benefits as an alternative to direct 3D imaging, have motivated this research.

1.2 Rationale

A high resolution SSM of the human scapula has been developed in the Division of Biomedical Engineering, University of Cape Town (Mutsvangwa et al., 2015). Additionally, a method of obtaining 3D coordinates of landmarks from bi-planar 2D calibrated X-ray images has been developed and validated (Chimhundu et al., 2014). It is thus feasible that 3D patient-specific approximations of the scapula bone can be obtained from 2D patient image data. A possible approach may be to register the 2D X-ray images of the scapula to the SSM directly to obtain a patient-specific 3D model of the scapula. However, this is a complex procedure and computationally expensive as it requires a number of optimisation parameters to produce an exact patient-specific 3D model (Markelj et al., 2012).

An alternative approach, followed in the research reported here, is manual selection of corresponding landmarks from the 2D X-ray images, followed by selection of the same landmarks on the shape model, and automatic transformation of the shape model into the 3D coordinate space defined by the calibrated 2D X-ray images. Using landmark-constrained SSM fitting, a SSM can be constrained to deform in a way that the model landmarks coincide with the reconstructed 3D landmarks from the 2D X-ray images. The approach includes extending the 2D-3D point localization method developed by Chimhundu et al. (2014) to a more user-friendly tool for X-ray stereophotogrammetry.

The scapula bone has been selected for this research as there is little in the literature on the scapula in this field. In addition, the scapula is considered to be a complex bone which forms an integral part of the shoulder complex (Peat et al., 2009). The shoulder complex provides the upper limb with a wide range of motion exceeding that of any other joint mechanism in the body (Lin et al., 2005). Methods developed on this bone may translate to other bones. Furthermore, the scapula bone is of specific interest in biomechanics as it plays a significant role in rehabilitation and diagnosis of shoulder injuries (Hulstyn and Fadale, 1997; Wilk et al., 2009; May and Bishop, 2013).

1.3 Objectives

The aim of this research was to design, develop and validate a 3D approximation tool of the scapula bone from 2D X-ray images using landmark-constrained SSM fitting. To achieve this aim and address the research problem, the following specific research objectives were formulated.

1. Develop an interactive graphical user interface (GUI) platform, to facilitate the automated fitting of a deformable 3D model to a set of user-defined 3D coordinates reconstructed from 2D X-ray images.
2. Perform a landmark reproducibility study to establish the most suitable anatomical landmarks on the 2D X-ray image and 3D model of a scapula bone that can be used for landmark-constrained SSM fitting.
3. Test and validate the developed tool using cadaveric image data, by comparison of the 3D approximation of a scapula bone to CT data, used as ground truth.

1.4 Overview of the reconstruction approach

The reconstruction approach was broken down into three stages: 1) X-ray stereophotogrammetry which aimed to reconstruct the 3D coordinates of points selected on bi-planar 2D X-ray images, 2) Landmark reproducibility based on the studies by Ohl et al. (2010) and Borotikar et al. (2015) to determine the reproducible landmarks of the scapula from lateral oblique and anteroposterior (AP) views, and 3) landmark-constrained SSM fitting which involved the use of Scalismo, an open source shape modelling platform developed by the University of Basel, Switzerland. This stage involved constraining an SSM to the reconstructed 3D coordinates (obtained from stage 1) of the selected reproducible landmarks (identified in stage 2) from 2D X-ray images.

1.5 Ethics

Ethics approval was granted, for the CT and X-ray scans of the subject (cadaveric shoulder), by the Human Research Ethics Committee (HREC) of the University of Cape Town (reference number HREC REF: 820/2015).

1.6 Dissertation Overview

The rest of this report is structured as follows. Chapter 2 presents a review of the literature on 3D medical imaging of bones. Chapter 3 discusses the theoretical concepts for the proposed landmark-based 3D approximations of bones. Chapter 4 presents X-ray stereophotogrammetry, the first stage of the research approach. Chapter 5 presents 3D localization validation, the last step of X-ray stereophotogrammetry in this project. Chapter 6 describes the second stage of the research approach namely landmark reproducibility, and Chapter 7 presents landmark-constrained SSM fitting, the last step in the research pipeline. Finally, Chapter 8 presents the recommendations for further work, limitations of this research and a summary of the findings, and concludes the report.

2 LITERATURE REVIEW

2.1 Shoulder complex and why we want to image it

The shoulder complex controls the position and movement of the upper limb in several directions to maintain shoulder stability (Sailer and Imhof, 2004). The complex movements and articulations of the components of the shoulder complex, namely the scapula, clavicle and humerus bones, make them vulnerable to several types of pathologies. These fractures include the coracoid process fracture (Zilberman and Rejovitzky, 1981), glenoid fracture (Warner and Dirksmeier, 1998), proximal-humerus fracture (Hedgson, 2006) and glenohumeral arthritis. The articulation points in the shoulder complex include the glenohumeral joint connecting the glenoid cavity of the scapula to the humerus, acromioclavicular joint connecting the scapula acromion to the clavicle and the scapulothoracic joint, an articulation point between the medial border of the scapula with the ribs (Figure 2.1).

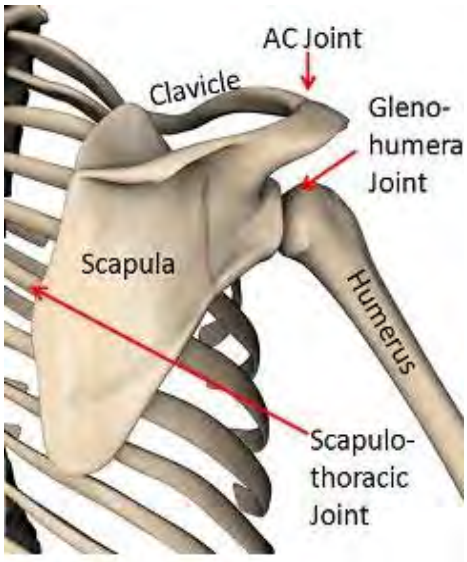

Figure 2.1: Major components of the shoulder complex. Acromioclavicular joint (AC), Scapulothoracic joint and the glenohumeral joint. Retrieved July 02, 2016 from http://www.physio-pedia.com/File:Scapulothoracic-joint.jpg. Copyright 2015 by Vanessa Rhule, adapted with permission.

The functional inter-relationships between the scapulothoracic, acromioclavicular and glenohumeral joints provide a full range of motion of the upper limb and any pathological condition of the scapula bone will disturb shoulder function (Kibler, 2015). Hence, the scapula bone plays a significant role in diagnosis and rehabilitation of shoulder injuries

(Voight and Thomson, 2000). This makes the shoulder one of the most common imaged parts of the upper limb.

2.2 Medical imaging of the shoulder complex

Three-dimensional imaging of bones is important as the 3D images and associated segmented models provide a concise visual representation of the bones and this facilitates diagnoses, treatment and surgical planning (Baka et al., 2011; Mantokoudis et al., 2013). Images of the shoulder can be acquired using 3D imaging modalities like magnetic resonance imaging (MRI) and X-ray computed tomography (CT).

Magnetic resonance imaging is a non-ionizing technique with full 3D imaging capabilities. Improvements in MRI hardware, scanning protocols and 3D volumetric reconstruction techniques have greatly increased the use of MRI for imaging hard tissue like the articular cartilage between bones (Varol et al., 2011) and the joints of shoulder complex (Steinbach, 2008). Magnetic resonance imaging produces excellent soft tissue contrast and high resolution 3D images (Gold et al., 2009).

X-ray CT was introduced to the medical field in 1972 (Kalender, 2006) and it is based on variable absorption of X-rays as they pass through different body tissue just like in conventional X-ray systems (Chapman et al., 2011). Computed tomography acquires a series of projections from many angles around the subject and the set of projections is then reconstructed via a back projection or equivalent algorithm (Xu and Wang, 2005) producing high resolution cross-sectional images. Computed tomography, however, uses ionisation radiation which can cause tissue damage and increases risk of cancer (Hall and Brenner, 2008).

Both CT and MRI can provide high resolution 3D medical volumetric images of the shoulder, but segmentation of these images to extract and analyse the scapula bone is tedious and time consuming. Furthermore, CT exposes the patient to higher levels of radiation than from 2D X-ray systems and the operational costs of MRI are higher than for 2D imaging. Despite the radiation exposure associated with the frequent use of CT and the higher operational and acquisition costs associated with MRI (Brenner and Elliston, 2004, Hall and Brenner, 2008), these modalities are preferable compared to 2D imaging systems like X-ray imaging because of the capability to produce 3D volumetric images of the shoulder. Three-dimensional images provide a realistic anatomical representation, whereas 2D X-ray images project overlapping

3D structures onto 2D image planes which limit the field of view. With a limited field of view, clinical operations like obtaining accurate measurements for treatment planning becomes difficult as depth information is lost, since the obtained measurements do not truly reflect spatial relationships between the anatomical landmarks (Chimhundu et al., 2014).

Three-dimensional representation of bone can also be obtained from single or multiple 2D X-ray images through the application of 2D-3D image reconstruction methods (Crum, 2004; Hassner and Rehovot, 2006; Gamage et al., 2009; Dworzak et al., 2010; Baka et al., 2011; Kotsas and Dodd, 2011). This can either be a registration of a patient's 3D data obtained from MRI or CT to the X-ray data or through the use of SSMs deformed to conform to the patient's anatomy.

2.3 2D-3D bone reconstruction

A detailed description of SSMs and how they can be used for 2D-3D bone reconstruction is presented below as this forms an integral component of the approach taken in this project.

2.3.1 Statistical shape models

Statistical shape models were first introduced by Cootes in 1989 (Cootes et al., 1992). Statistical shape model development is generally based on a training dataset that provides the model with a priori knowledge about the expected shape distribution of the object. The uses for SSMs include segmentation of medical images (Heimann and Meinzer, 2009) and they are widely used to create deformable patient-specific models (Gamage et al., 2009; Heimann and Meinzer, 2009; Mutsvangwa et al., 2015) that can be used in medical procedures like pre-operative planning. They have recently become ubiquitous in 3D reconstruction from 2D images, through establishing correspondences between the 2D image and the SSM (Laporte et al., 2003; Pomero et al., 2004; Kurazume et al., 2009; Zheng et al., 2009; Dworzak et al., 2010). Active shape model (Cootes et al., 1995) and active appearance model (Matthews and Baker, 2004) algorithms are the best known methods that are used to fit SSMs to a new set of 2D or 3D images. Different approaches exist in the literature as presented below.

2.3.2 Statistical shape model based 2D-3D reconstruction techniques

Many researchers have investigated different methods of using SSMs for 2D-3D reconstruction of different anatomical body parts (Pomero et al., 2004; Kurazume et al., 2009; Zheng et al., 2009; Dworzak et al., 2010; Baka et al., 2011). The methods often use two or more X-ray image perspectives for the reconstruction. The methodological approaches for

the reconstruction can be separated into feature-based and intensity-based approaches as presented below.

Feature-based reconstruction algorithms are based on correspondence between image features such as landmarks, edges, and contours. Laporte et al. (2003) presented a 3D reconstruction algorithm based on contour identification from bi-planar 2D radiographs of the femur. They compared the contours to 2D projections of corresponding 3D contours on a single model of the femur. Comparison of the femoral reconstructions to 3D CT scan ground truth data yielded a mean distance error of 0.7 mm.

Pomero et al. (2004) used a semi-automated 3D reconstruction algorithm using vertebral body volume reconstruction by definition a local referential associated with the volume. Furthermore, a SSM was used to obtain reliable prior knowledge of the vertebral shape. The reconstruction algorithm was based on dry normal and scoliotic vertebral models. The 3D coordinates of each model, which were derived from manual measurements, were used to define a template or basic vertebral shape. Comparison of the lumbar spine reconstruction with corresponding CT-derived 3D ground truth data, resulted in an average surface-to-surface distance of 1.40 mm between the two 3D models.

Kurazume et al. (2009) presented a method to estimate a patient-specific 3D model of a femur from two fluoroscopic images using a parametric model constructed from SSMs. The pose and shape parameters of the model were estimated using a distance map obtained through a level set approach (Iwashita et al., 2004). Comparison of the reconstructed femur model with corresponding 3D CT reconstructions, resulted into an average error of 0.95 mm between the estimated shape and actual shape.

Zheng et al. (2009) presented a 2D-3D correspondence building method based on a non-rigid 2D matching process to develop a patient-specific 3D model of the femur from X-ray images. Their reconstruction algorithm used a symmetric injective nearest-neighbour mapping operator and deformation based on 2D thin-plate splines (Sibson and Stone, 1991). The thin-plate splines were used to find best matched 2D point pairs between features extracted from the 2D images and those extracted from the 3D model. This algorithm generated an error of 1.10 mm when compared with corresponding CT data from cadaveric specimen.

Dworzak et al. (2010) worked on a 3D reconstruction of the human rib cage from 2D projection images using SSMs. Their work addressed two problems: (1) the 3D shape reconstruction of an individual rib cage and, (2) its 3D pose reconstruction from bi-planar 2D

X-ray images. This technique yielded an average error of 2.2 mm for the 3D surface distance between the reconstructed model and a CT ground truth model.

Baka et al. (2011) combined a 3D distance-based objective algorithm with automatic edge identification on a Canny edge map in the projection images to reconstruct a 3D shape of a femur from X-ray images using SSMs. Comparison of the reconstructed 3D shape with the CT ground truth resulted in a reconstruction accuracy of 0.68 mm point-to-surface distance.

Intensity-based reconstruction algorithms register the entire image to the target image. This approach can be used to overcome the possibility of using incorrect correspondences. Hurvitz et al. (2008) used digitally reconstructed radiographs (DRRs) to establish correspondences between fluoroscopic images and a SSM. The registration of the model to the fluoroscopic images was performed in a recursive process until the convergence condition was satisfied for the best transformation estimates. A mean surface approximation error of 0.85 mm was obtained, on comparison of the reconstructed shape and CT ground truth of the femur.

Tang et al. (2005) used a hybrid 3D model to reconstruct 3D surfaces from two to four 2D X-ray projections of the object. Results of simulated projections and fluoroscopic images of distal femurs showed that the images could be registered with an accuracy of about 2 mm.

2.4 Summary of the review of 3D imaging of bones

In summary, two approaches of acquiring 3D medical images of bones were presented. The first approach involves the use of 3D imaging systems like MRI and CT to directly obtain 3D patient images of the region of interest. However, this tends to be expensive and the higher ionization radiation exposures from CT present a cancer risk (Hall and Brenner, 2008).
The second approach utilizes various methods to reconstruct 3D patient-specific models from 2D images (X-ray or fluoroscopy). Different methods have been reviewed using model-based 2D-3D reconstruction algorithms but most of these algorithms and methods have been developed for the femur (Laporte et al., 2003; Zheng et al., 2009; Yokota et al., 2009, Kurazume et al., 2009). Reports of model-based 2D-3D registration for other bones in the body particularly for the upper limbs are scarce in the literature. Up to now there have been none for the scapula, for example, due to the complexity of the bone and also the superposition of various other bone structures surrounding the scapula. Furthermore, most of the methods reviewed in this literature tackle the 2D-3D reconstruction problem in the 2D/3D domain and are based on registration of a 2D image to a 3D image. Other approaches that turn the reconstruction problem into a 3D-3D reconstruction paradigm should be explored.

3 THEORETICAL CONCEPTS FOR LANDMARK-BASED 3D APPROXIMATION

3.1 Overview

In this project the reconstruction of the 3D object is treated as a 3D to 3D problem by taking advantage of 3D landmark localization from X-ray stereophotogrammetry. Given two or more 2D images from X-ray scans, the position of a 3D point can be obtained from the intersection of the projection rays of the 2D images using X-ray stereophotogrammetry (Chimhundu et al., 2014). Different researchers have developed different X-ray stereophotogrammetry techniques (Adams, 1981; Douglas et al., 2004; Chimhundu et al., 2014) that are used to obtain the 3D coordinates of points selected on digital low-dose 2D X-ray images. Once the landmarks are obtained in 3D, these are then used to constrain a SSM in the sparse fitting procedure.

It has been established in the literature review that SSMs use morphological models to achieve full shape reconstructions from 2D images. This is as an alternative to having only 3D position localizations of the image points (Douglas et al., 2004; Chimhundu et al., 2014). It has the potential to provide high quality patient-specific 3D models from 2D X-ray images.

Additionally the project leverages the use of a low dose X-ray imaging system to minimize the dose to the patient during the X-ray acquisitions. The X-ray images are obtained using low-dose 2D imaging provided by the Lodox Statscan imaging system (Lodox Systems, South Africa).

The 3D approximation of scapula bone from 3D landmarks obtained from 2D X-ray images may be broken down into three stages: 1) X-ray stereophotogrammetry, 2) landmark reproducibility, and 3) landmark-constrained SSM fitting (Figure 3.1). X-ray stereophotogrammetry involves the reconstruction of 3D coordinates of points selected on 2D X-ray images. The theoretical frame work of X-ray stereophotogrammetry discussed in this report is based on low-dose digital images obtained using Lodox Statscan system (section 3.2). Landmark reproducibility discusses the reproducible landmarks on a scapula image and model. Landmark-constrained SSM fitting describes the techniques used to fit a SSM on to a set of 3D coordinates obtained from a 2D X-ray image.

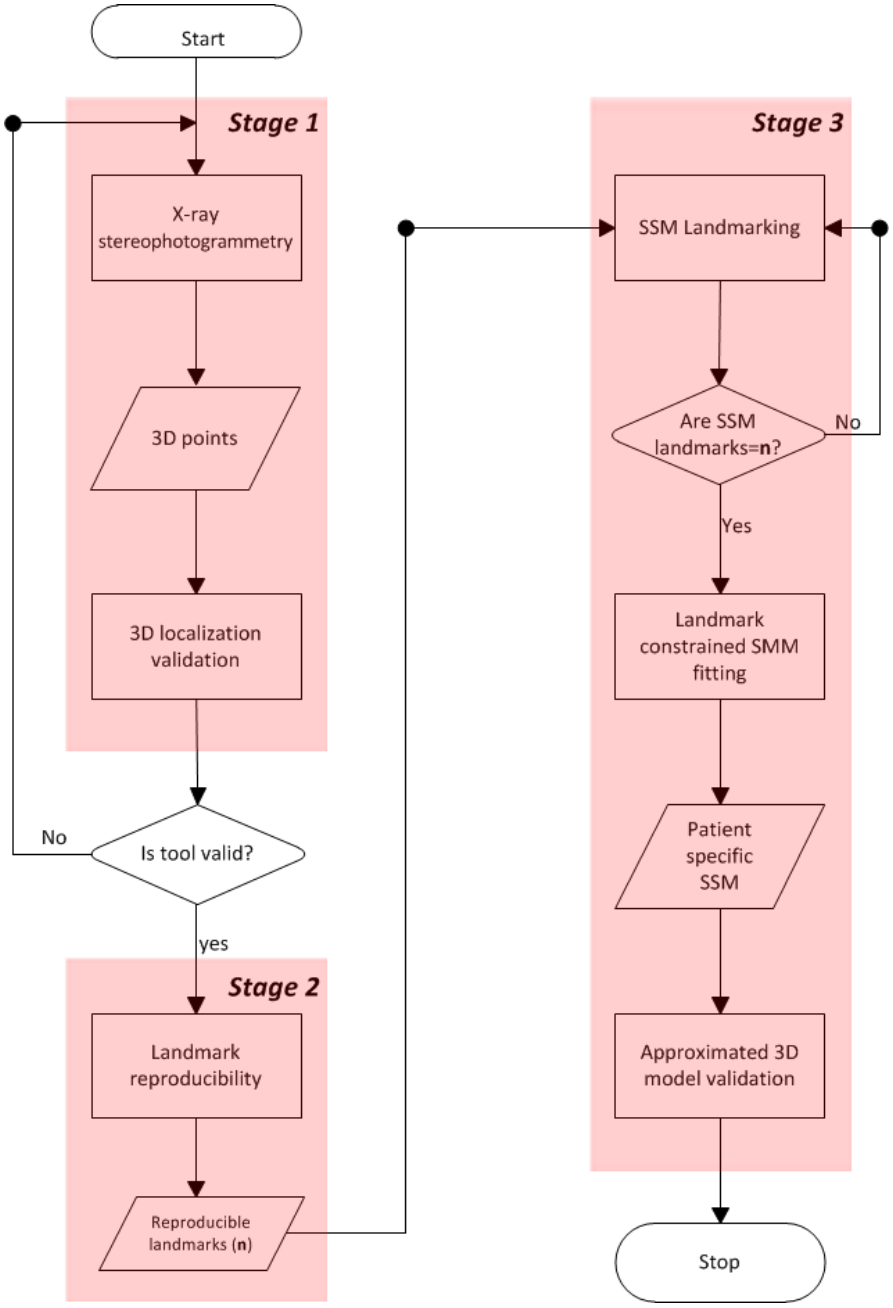

Figure 3.1: Stages of 3D approximation of scapula bone shape from 2D X-ray images using landmark-constrained SSM fitting. X-ray stereophotogrammetry (stage 1), Landmark reproducibility (stage 2) and landmark-constrained SSM fitting (stage 3).

3.2 2D X-ray imaging on Lodox Statscan system

The Lodox Statscan system utilises a fan beam that only varies in the slit direction (width of region of interest), but is very narrow in the scan direction. This is different from conventional X-ray imaging systems that use a cone beam shape that varies in both slit and scan directions (Figure 3.2). This results in the Lodox Statscan delivering less radiation dose compared to conventional X-ray imaging systems (Irving et al., 2008).

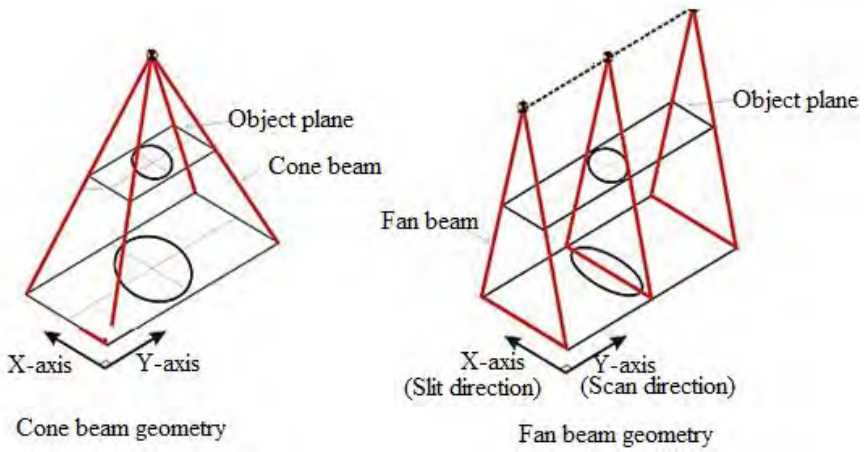

Figure 3.2: Comparison of the X-ray beam geometries used by the conventional X-ray systems and Lodox Statscan system.

The Lodox Statscan system has a C-arm that rotates between vertical and horizontal directions (Figure 3.3) enabling scans to be captured at any angle within the range 0^0 to 90^0. This provides a wider anatomical view of areas of interest for image analysis. Additionally this configuration offers a number of advantages:

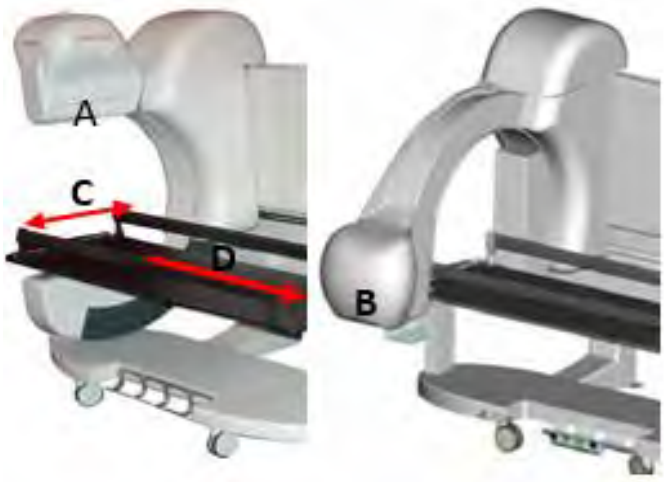

Figure 3.3: Lodox Statscan: (A) C-arm in vertical position, (B) C-arm in horizontal position, (C) Slit direction and (D) Scan direction. Retrieved June 30, 2016 from http://radiologykey.com/trauma-radiography/. Courtesy Lodox Systems [Pty], Ltd.

- The narrow fan beam consists of mostly primary X-rays hence scattered radiation is very low making it safe for the patient and the radiographer (Irving et al., 2008).
- Conventional X-ray systems abide by the inverse square law, which states that the radiation intensity output is inversely proportional to the square of the distance from the source (Wanser et al., 2012) given by:

$$I = \frac{1}{r^2} I_0 \qquad [3.1]$$

In equation [3.1], ***I*** is the radiation intensity output at a given distance ***r*** from the source, and ***I₀*** is the original radiation intensity. Linear slot scanning radiography, as used by the Lodox Statscan system, ensures that the radiation intensity is given by:

$$I = \frac{1}{r} I_0 \qquad [3.2]$$

This implies that a lower radiation source (***I₀***) is utilised by the Lodox to produce the same radiation dose, at the same distance (***r***), as the conventional X-ray systems.

3.3 Methods used in X-ray stereophotogrammetry

3.3.1 3D Projective transformations

Projective transformations are a variation of direct linear transformation (DLT), a triangulation method developed by Abdel and Karara (1971). Projective transformation algorithms have been successfully used for 3D point localization from X-ray by different researchers, including Adams (1981), Douglas et al. (2004) and Chimhundu et al. (2014), with reconstruction errors of (0.90, 1.00 and 0.68) mm respectively. In this project the projective transformation algorithm by Adams (1981) and modified by Chimhundu et al. (2014) to suit Lodox Statscan imaging geometry is presented. The details of the modification are described in the sections below.

3.3.2 Derivation of 3D projective transformations

A 3D projective transformation defines a correspondence between real-world coordinates (**X, Y, Z**) and image points (**u, v**) by the utilization of transformation parameters which map the image point to the corresponding 3D real-world coordinates (Adams, 1981). Transformation parameters are obtained through a volume calibration. Calibration is the estimation of some mathematical parameters of a system using reference parameters to numerically solve for the unknown parameters (Zhang, 2004). Adams (1981) defined a projective transformation that maps image points to real-world coordinates as:

$$u = \left[\frac{b_{11}X + b_{12}Y + b_{13}Z + b_{14}}{b_{21}X + b_{22}Y + b_{23}Z + 1} \right] \;,\; v = \left[\frac{b_{31}X + b_{32}Y + b_{33}Z + b_{34}}{b_{41}X + b_{42}Y + b_{43}Z + 1} \right] \qquad [3.3]$$

In equation [3.3]**, X,Y,Z** are known reference points in a 3D space and $\mathbf{b_{ij}}$ are the transformation parameters. During calibration, the objective is to find these transformation parameters. Given bi-planar 2D images with points (***u, v***) and ($\boldsymbol{u^i}$, $\boldsymbol{v^i}$) from the first and

second views respectively aquired using Lodox Statscan system, the 2D-3D correspondances for the first view can be calculated from the equations [3.4] and [3.5] derived from equation [3.3] (Appendix A).

$$u = b_{11}X + b_{12}Y + b_{13}Z + b_{14} - b_{21}uX - b_{22}uY - b_{23}uZ \quad [3.4]$$

$$v = b_{31}X + b_{32}Y + b_{33}Z + b_{34} - b_{41}vX - b_{42}vY - b_{43}vZ \quad [3.5]$$

Similary, the 2D-3D correspondances for the second view can be established using equations [3.6] and [3.7].

$$u^i = b^i{}_{11}X + b^i{}_{12}Y + b^i{}_{13}Z + b^i{}_{14} - b^i{}_{21}u^iX - b^i{}_{22}u^iY - b^i{}_{23}u^iZ \quad [3.6]$$

$$v^i = b^i{}_{31}X + b^i{}_{32}Y + b^i{}_{33}Z + b^i{}_{34} - b^i{}_{41}v^iX - b^i{}_{42}v^iY - b^i{}_{43}v^iZ \quad [3.7]$$

In equations [3.6] and [3.7], $\mathbf{b^i_{ij}}$ are the transformation parameters for the second view.

3.3.3 Derivation of transformation parameters

Transformation parameters that map the image points (***u, v***) and (***u^i, v^i***) from the first and second views to their corresponding **X,Y,Z** real world coordinates are compuated from equations [3.4] – [3.5] and [3.6] – [3.7] respectively. The relationship between the (**X, Y, Z**) real-world coordinates and the **(u)** image coordinates is established through a 7 × 1 matrix, $\mathbf{B_u}$, which defines the transformation parameters for the **u** image coordinate in the first view. This relationship is established through equation [3.8] which defines the eight point algorithm (R. I. Hartley, 1997).

$$\begin{bmatrix} x & y & z & 1 & -u_1x & -u_1y & -u_1z \\ x & y & z & 1 & -u_2x & -u_2y & -u_2z \\ \vdots & \vdots & \vdots & \vdots & \vdots & \vdots & \vdots \\ x & y & z & 1 & -u_nx & -u_ny & -u_nz \end{bmatrix} * \begin{bmatrix} b_{11} \\ b_{12} \\ b_{13} \\ b_{14} \\ b_{21} \\ b_{22} \\ b_{23} \end{bmatrix} = \begin{bmatrix} u_1 \\ u_2 \\ \vdots \\ u_n \end{bmatrix} \quad [3.8]$$

$$\mathbf{F_u * B_u = G_u} \quad [3.9]$$

Similarly, a relationship between (**X, Y, Z**) real-world coordinates and the **(v)** image coordinates is established through a 7 × 1 matrix, $\mathbf{B_v}$, which defines the transformation parameters for the **v** image coordinates in the first view given by equation [3.10].

$$\begin{bmatrix} x & y & z & 1 & -\mathrm{v}_1 x & -v_1 y & -v_1 z \\ x & y & z & 1 & -v_2 x & -v_2 y & -v_2 z \\ \vdots & \vdots & \vdots & \vdots & \vdots & \vdots & \vdots \\ x & y & z & 1 & -v_n x & -v_n y & -v_n z \end{bmatrix} * \begin{bmatrix} b_{31} \\ b_{32} \\ b_{33} \\ b_{34} \\ b_{41} \\ b_{42} \\ b_{43} \end{bmatrix} = \begin{bmatrix} v_1 \\ v_2 \\ \vdots \\ v_n \end{bmatrix} \quad [3.10]$$

$$\mathbf{F_v} * \mathbf{B_v} = \mathbf{G_v} \quad [3.11]$$

The transformation parameters $\mathbf{b_{ij}}$ for the first view can then be calculated from eqautions [3.9] and [3.11] by solving for matrix $\mathbf{B_{u.}}$and $\boldsymbol{B_v}$ respectively. Matrix $\mathbf{B_{u.}}$ is obtained through computing the product of matrix $\mathbf{G_u}$ and the inverse of matrix $\mathbf{F_u}$. Matrix $\mathbf{B_v}$ is obtained through computing the product of matrix $\mathbf{G_v}$ and the inverse of matrix $\mathbf{F_v}$. Similar equations can be setup for the second view.

3.3.4 3D point localization

Three-dimensional point localization allows for location of points in 3D space given two or more views. This can be achieved through the use of transformation parameters for a calibrated scene or 3D pose estimation for an uncalibrated scene using techniques like Pose from Orthography and Scaling with Iterations (POSIT) (Kelley et al., 2015). For a calibrated scene, mathematical algorithms which make it possible to solve a system of linear equations containing the transformation parameters and reference points have been developed. One of the most common algorithms is the Gaussian elimination method using back substitution (Higham, 2011).

Back substitution is a process of solving a linear system of equations that have been transformed into row-echelon form (Aldroubi and Sekmen, 2014). The equations are manipulated in such a way that the unknowns are eliminated until only a single unknown is obtained in the last equation. The last equation is then solved first, the output is then used for the next equation, and then the next until all the unknowns are solved for. The back substitution method has been used for solving systems of equations by different researchers in X-ray stereophotogrammetry, including Adams (1981) for determining 3D position of points in an image, Douglas et al. (2004) for 3D point localization in low-dose 2D X-ray images, Sawyer et al. (2009) for 3D stereophotogrammetry quantitative analysis of the lip

and Chimhundu et al. (2014) for inter-landmark measurements of images from Lodox Statscan system.

3.3.5 Epipolar geometry

Epipolar geometry is an intrinsic geometry between two plane views that helps to establish a relationship between the matching image points in the views. Epipolar geometry simplifies searches for corresponding points between views (Zhang et al., 2010).

Suppose ***x*** is the image point in the first view, the corresponding image point in the second view lies on an epipolar line $\boldsymbol{l^1}$ (Figure 3.4) (Basta, 2014). The epipolar line intersects the epipolar plane and the image plane. The epipolar plane is defined by a 3D point, ***p*** and the centres of projection; **0** and **0'** (Figure 3.4). The epipolar geometry can be computed using either an essential matrix (Helmke et al., 2007) or a fundamental matrix (Hartley and Zissermann, 2009). In a calibrated environment, the depth information from a pair of images can be obtained geometrically by using an essential matrix whereas in an un-calibrated environment, the fundamental matrix is utilised.

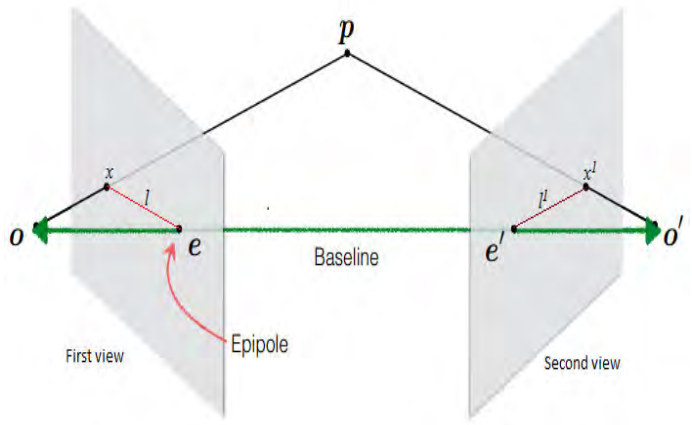

Figure 3.4: Epipolar constraint relating a point, x in the first view to the corresponding point, x^i in the second view, adopted from Basta (2014).

Given a point, ***p***, with image coordinates (**u, v**) in the first view and ($\mathbf{u^i}$, $\mathbf{v^i}$) in the second view, the two image coordinates from both views are related by a fundamental matrix, ***F*** given by:

$$(u, v, 1) * F * \begin{pmatrix} u^i \\ v^i \\ 1 \end{pmatrix} = 0 \qquad [3.12]$$

In equation [3.12], ***F*** is a 3 × 3 matrix defined by:

$$F=\begin{bmatrix} f11 & f12 & f13 \\ f21 & f22 & f23 \\ f31 & f32 & f33 \end{bmatrix} \quad [3.13]$$

In an uncalibrated space, the fundamental matrix, ***F*** can be computed using the eight point algorithm (Hartley, 1997) which requires eight control points given by equation [3.14].

$$\underbrace{\begin{bmatrix} u_1u_1^i & u_1v_1^i & u_1 & v_1u_1^i & v_1v_1^i & v_1 & u_1^i & v_1^i & 1 \\ u_2u_2^i & u_2v_2^i & u_2 & v_2u_2^i & v_2v_2^i & v_2 & u_2^i & v_2^i & 1 \\ u_3u_3^i & u_3v_3^i & u_3 & v_3u_3^i & v_3v_3^i & v_3 & u_3^i & v_3^i & 1 \\ u_4u_4^i & u_4v_4^i & u_4 & v_4u_4^i & v_4v_4^i & v_4 & u_4^i & v_4^i & 1 \\ u_5u_5^i & u_5v_5^i & u_5 & v_5u_5^i & v_5v_5^i & v_5 & u_5^i & v_5^i & 1 \\ u_6u_6^i & u_6v_6^i & u_6 & v_6u_6^i & v_6v_6^i & v_6 & u_6^i & v_6^i & 1 \\ u_7u_7^i & u_7v_7^i & u_7 & v_7u_7^i & v_7v_7^i & v_7 & u_7^i & v_7^i & 1 \\ u_8u_8^i & u_8v_8^i & u_8 & v_8u_8^i & v_8v_8^i & v_8 & u_8^i & v_8^i & 1 \end{bmatrix}}_{Z} * \underbrace{\begin{bmatrix} f_{11} \\ f_{12} \\ f_{13} \\ f_{21} \\ f_{22} \\ f_{23} \\ f_{31} \\ f_{32} \\ f_{33} \end{bmatrix}}_{F} = 0 \quad [3.14]$$

In equation [3.14, matrix **Z** contains known (***u, v)*** and (***u^i, v^i)*** images coordinates obtained from the first and second views respectively. The fundamental matrix, ***F*** is computed as a least square solution (Allen et al., 2014) of the singular value decomposition (SVD) of matrix ***Z.***

In a calibrated scene, the epipolar geometry is established using an essential matrix, ***E*** that relates the image point (**u, v**) from the first view to the corresponding image point (**u^i, v^i**) in the second view as shown in equation [3.15] (Horn, 1990).

$$(u, v, 1) * E * \begin{pmatrix} u^i \\ v^i \\ 1 \end{pmatrix} = 0 \quad [3.15]$$

With known transformation parameters, matrix **E** can be given by:

$$E = S * P^i * P_{inv} \quad [3.16]$$

where $\mathbf{P_{inv}}$ is the inverse of matrix, **P** which is a projection matrix containing the transformation parameters for the first view obtained from equations [3.8] and [3.11], $\mathbf{P^i}$ is the projection matrix containing the transformation parameters for second view and **S** is a skew symmetric matrix (Mackey et al., 2013) given by:

$$S = \begin{bmatrix} 0 & -a3 & a2 \\ a3 & 0 & -a1 \\ -a2 & a1 & 0 \end{bmatrix} \quad [3.17]$$

where $\mathbf{a}_i$ are the elements of a 1 × 3 matrix, **A,** given by, $\mathbf{A} = \mathbf{P^i} * \mathbf{P_{null}}$. $\mathbf{P_{null}}$ is the null space of the projection matrix **P** (Coleman and Pothen, 1986). The skew matrix is used to draw the epipolar line in the corresponding view.

3.4 Validation of reconstructed 3D points

Different researchers have investigated different tests for validating reconstructed 3D coordinates from X-ray stereophotogrammetry (Douglas et al., 2004; Chimhundu et al., 2014). These include the control point and test point reconstruction tests.

3.4.1 Control point reconstruction

Control point reconstruction involves the use of the control points used in the calculation of the transformation parameters to reconstruct the known 3D coordinates. Control point reconstruction is used to measure the mathematical correctness of a 2D-3D reconstruction algorithm (Douglas et al., 2004). Reconstruction errors (e_x, e_y, e_z) in (**X, Y** and **Z)** coordinates respectively between the reconstructed coordinates and the known 3D coordinates of the control points can be calculated using equations [3.18] – [3.20] (L. Chen, 1994). The resultant reconstruction error, $\mathbf{E_i}$ for the $\mathbf{i^{th}}$ point for **n** number of measurements can be calculated using equation [3.21].

$$e_x = \frac{1}{n}\sum_{i=1}^{n} | X_{ri} - X_{ei} | \quad [3.18]$$

$$e_y = \frac{1}{n}\sum_{i=1}^{n} | Y_{ri} - Y_{ei} | \quad [3.19]$$

$$e_z = \frac{1}{n}\sum_{i=1}^{n} | Z_{ri} - Z_{ei} | \quad [3.20]$$

$$E_i = \sqrt{(X_{ri} - X_{ei})^2 + (Y_{ri} - Y_{ei})^2 + (Z_{ri} - Z_{ei})^2} \quad [3.21]$$

In equations [3.18] - [3.21], ($\mathbf{X_{ri}}$, $\mathbf{Y_{ri}}$, $\mathbf{Z_{ri}}$) and ($\mathbf{X_{ei}}$, $\mathbf{Y_{ei}}$, $\mathbf{Z_{ei}}$) are the known 3D coordinates and reconstructed coordinates of the control points respectively.

3.4.2 Test point reconstruction

Test point reconstruction is a testing method that involves the reconstruction of points with known 3D coordinates but that have not been used for the calculation of the transformation parameters. Test point reconstruction is used to measure system performance (Douglas et al., 2004). If the known 3D coordinates of the test points are obtained using the same coordinate system as the reconstructed 3D coordinates, then reconstruction errors (e_x, e_y, e_z) in (**X, Y** and **Z)** coordinates respectively between the reconstructed coordinates and the known 3D coordinates of the test points can be calculated using equations [3.18] – [3.20]. However, if different coordinate systems are used, inter-landmark distances (ILD) (section 3.7.4) between points can be compared. This is calculated using equation [3.34].

3.5 Landmark reproducibility

3.5.1 Reproducible landmarks of the scapula image and model

Reproducible landmarks are points that can be repeatedly selected either by the same individual or by someone else working independently. Several studies (Ohl et al., 2010; Schwartz et al., 2011; Borotikar et al., 2015) show that there are reproducible scapula landmarks. Ohl et al. (2010) reported the coracoid process, the inferior glenoid rim and the lateral border as reproducible landmarks on the scapula (Figure 3.5) in a study on locating shoulder bony landmarks.

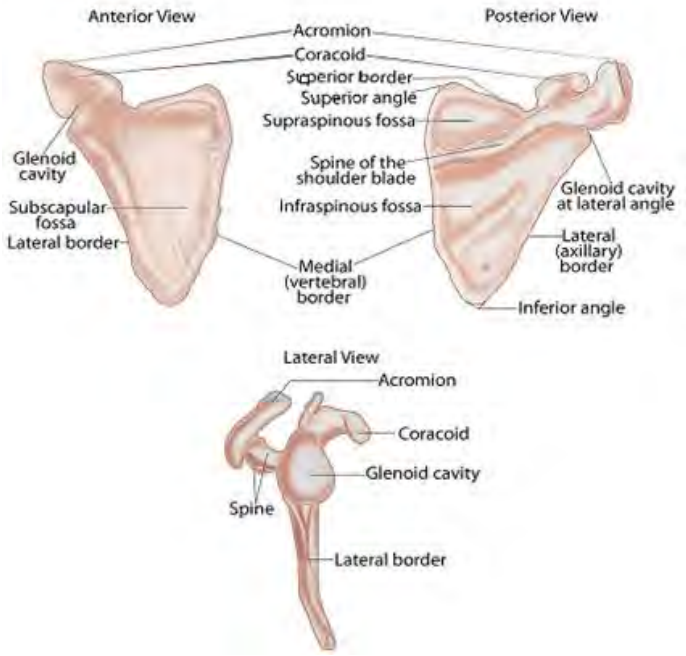

Figure 3.5: Anatomical landmarks of the scapula. Retrieved July 03, 2016, from http://www.ehealthstar.com/anatomy/shoulder-blade-scapula#comment-97724. Copyright 2016 by Jan Modric, adapted with permission.

Schwartz et al. (2011) reported the acromial angle, root of the scapula spine and the inferior angle of the scapula as the most reproducible landmarks during a reproducibility and repeatability study of upper limb landmark palpation for junior operators.

Reproducible landmarks of the scapula serve as anatomical reference points, making them good candidate points for X-ray stereophotogrammetry (Douglas et al., 2004). The reproducible landmarks of the scapula image used in this project are explored in chapter 6 as they form an integral component of this research.

The study on clinical validation and reliability of landmark selection of an anatomically augmented SSM of the scapula by Borotikar et al. (2015) shows good reproducibility for the tip of the coracoid process, the inferior glenoid rim, the lateral border ,landmarks around the glenoid rim and the borders of the scapula model (Figure 3.6). Biomechanical and medical image analysis of the scapula requires precise identification of the scapula reproducible and reliable landmarks as they are necessary to define the glenohumeral and acromioclavicular joints coordinate systems and in kinematics (Ohl et al., 2010).

The reproducible landmarks on a scapula are also a good candidate points for fitting algorithms like landmark-constrained SSM fitting, an approach explored in Chapter 7.

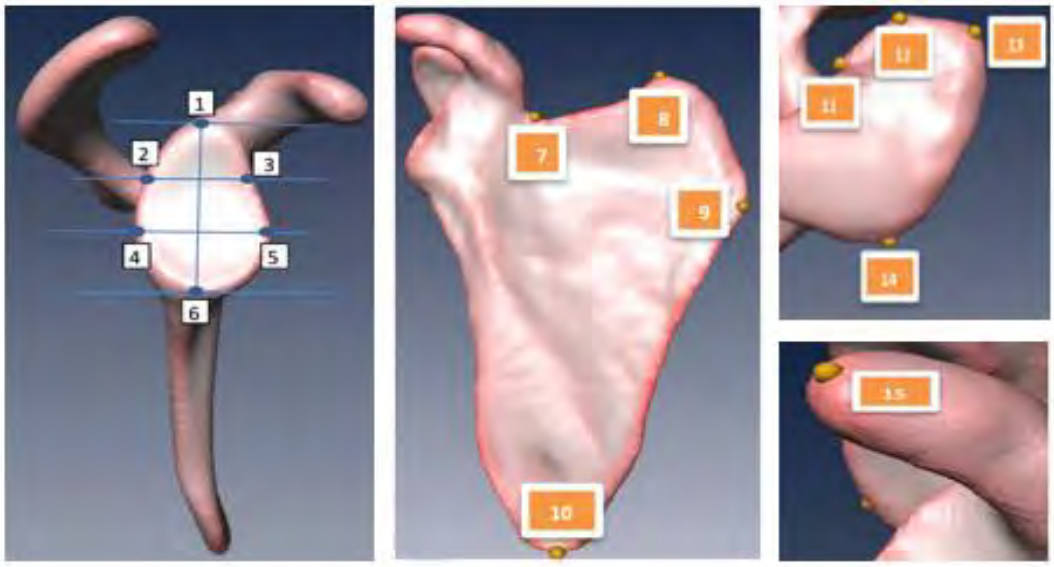

Figure 3.6: Reproducible landmarks on a scapula model: (1) Superior glenoid rim, (6) Inferior glenoid rim, (7) Suprascapula notch, (8) Superior angle, (9) Base of scapula spine, (10) Inferior angle, (13) Tip of acromion, (15) Tip of coracoid process (Borotikar et al., 2015).

3.6 Methods used in landmark-constrained SSM fitting

Landmark-constrained SSM fitting involves registering landmarks of a SSM to the corresponding landmarks of an image such that there is consistent and clear correspondence between the model and image landmarks (Sotiras et al., 2013). With established landmark correspondences, the model can be fitted on the image landmarks.

During landmark-constrained SSM fitting, the fitting objective is to obtain a likelihood function matching the model landmark parameters with the image landmark parameters to ensure that all align and minimises the misalignment error between them (Saragih et al., 2011). The registration problem is to determine a domain warp, H(**p**) (Figure 3.7) that maps the selected landmarks on the SSM ($\mathbf{M_L}$) to the 3D image coordinates ($\mathbf{T_L}$) to ensure point to point correspondences such that $L = \{(l_1^M, l_1^T), (l_2^M, l_2^T), \cdots, (l_n^M, l_n^T)\}$ where l_i^M is the ***i*th** model landmark, l_i^T is the ***i*th** target landmark and **L** defines the landmark correspondences for **n** landmarks (Lüthi et al., 2011).

The likelihood function given the correspondences can be defined using a gaussian process regression such that:

$$p(L \mid \mathrm{u}) = \prod_{\mathrm{i=1}}^{\mathrm{N}} \mathrm{N}(u(x), \sigma^2) \qquad [3.22]$$

In equation [3.22], $u(x)$ is the deformation field given the observation (landmark correspondences) and σ is a noisy assumption that is used to control deformation accuracy (Lüthi et al., 2011) .

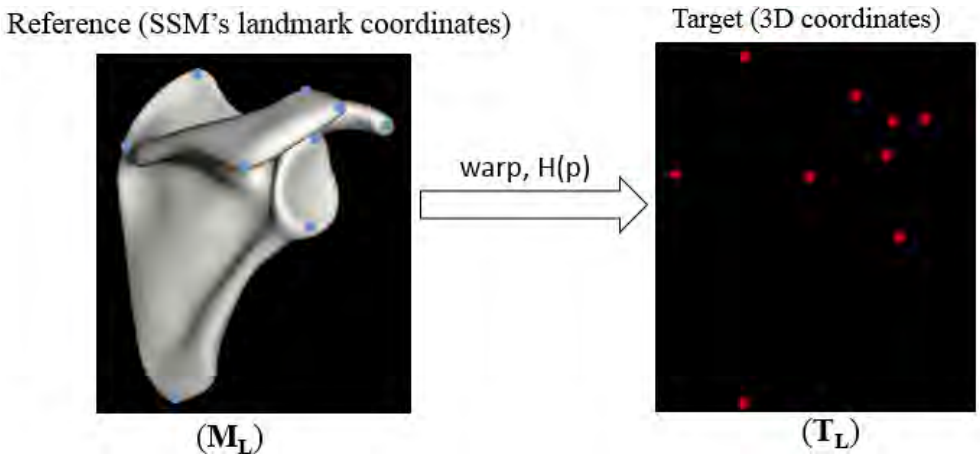

Figure 3.7: Landmark-constrained SSM fitting. $\mathbf{M_L}$ are the selected landmark's 3D coordinates on the SSM (blue) and $\mathbf{T_L}$ are the target 3D coordinates (red)

The landmark correspondences establish a confidence region giving information about where the likely shape could possibly lie. The produced model will have no variance in the confidence region, hence constrained at these points. However, a lot of variance can still exist in other regions. The produced model is therefore a Gaussian process model (section 3.6.2) which has the property that all the shapes that can be explained by the model somehow match the observation. This model is called the posterior model (section 3.6.3) whose mean defines the best deformation field given the observation. Methods used in landmark-constrained fitting are discussed below.

3.6.1 Transformations in landmark-constrained SSM fitting

Given a reference SSM, $\boldsymbol{M_L}$ and target image landmarks $\boldsymbol{T_L}$, a landmark-constrained SSM fitting process aims at obtaining a spatial transformation matrix $\boldsymbol{H\,(p)}$, where $P^T = (p_1,\ldots,p_n)$ are transformation parameters that map the model landmarks to the image landmarks such that:

$$M_L\,(H\,(p)) \approx T_L \qquad [3.23]$$

Transformations used in image processing can be classified into rigid or non-rigid transformations. Rigid transformations are a type of transformation that preserve the size and shape of the image. The pre-image and the transformed image are congruent (Challis, 1995). The three basic forms of rigid transformations, include reflections, rotations and translations (Figure 3.8). A rigid transformation acting on a vector $\boldsymbol{v}$ produces a transformed vector, $T(v)$ such that:

$$T(v) = Rv + t \qquad [3.24]$$

In equation [3.24], $R^{\mathrm{T}} = R^{-1}$. $\boldsymbol{R}$ defines a linear transformation (Abdel and Karara, 2015) and $\boldsymbol{t}$ is a vector that gives a translation to the origin.

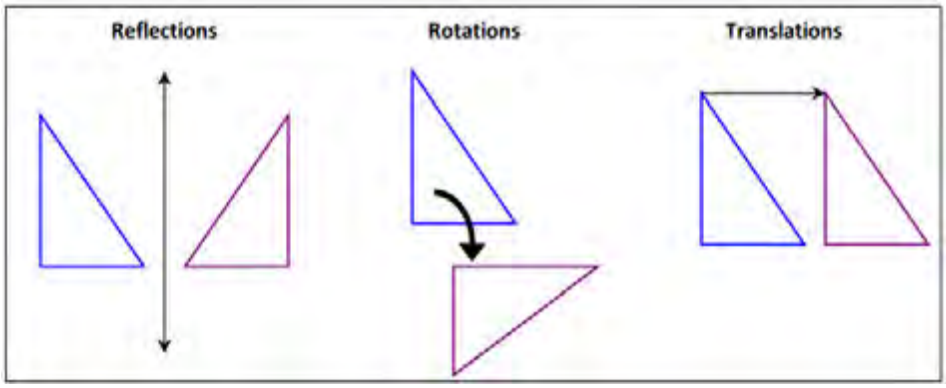

Figure 3.8: Illustration of the effect of reflection, rotation and translation on a shape.

Rigid transformations are used to determine the relationship between two coordinate systems. This has application in stereophotogrammetry, pose estimation and in object motion analysis.

A non-rigid transformation, unlike rigid transformation, defines any transformation of a geometric object that changes its size but preserves the shape (Crum et al., 2004). Examples of a non-rigid transformation include vertical and horizontal stretching or shrinking and dilation. Non-rigid transformations are commonly used in computer vision, pattern recognition, medical imaging, motion correction, morphometry and segmentation (Crum et al., 2004).

3.6.2 Gaussian processes

A Gaussian process is an extension of a multivariate normal distribution (Muirhead, 2008) to a distribution over functions. Gaussian processes are more general than the standard multivariate normal distribution as they can be applied to an infinite number of points. This can be achieved with the ability to define the mean and covariance functions of the Gaussian process.

A Gaussian process, $GP(\mu, k)$ is simply defined by its mean, $\mu : \Omega \to \Re^2$ and covariance, $k : \Omega * \Omega \to \Re^{2*2}$ functions. The mean function defines the mean deformation $\mu(x)$ for every point $x \in \Omega$ and the covariance function defines the covariance $k(x, x^i)$ between any deformations for points x and x^i (Ledoit and Wolf, 2004). Gaussian processes are commonly used in statistics and machine learning. In machine learning, they can be used in Bayesian numerical analysis and uncertainty quantification (Bilionis and Zabaras, 2012). Gaussian processes have recently been used at the University of Basel, Switzerland for shape modelling to model shape deformations (Lüthi et al., 2011).

Given a point **x**, Gaussian processes may be used to define deformations at point **x** as:

$$u(x) = \begin{pmatrix} u_1(x) \\ u_2(y) \end{pmatrix} \qquad [3.25]$$

where $u(x)$, $u_1(x)$ and $u_2(y)$ are the deformations at point **x**, in the **X**-direction and in the **Y**-direction respectively. To specify the model deformations fields, the mean and covariance functions can be used such that:

$$u(x) = \left(\begin{pmatrix} \mu_1(x) \\ \mu_2(y) \end{pmatrix}, \begin{pmatrix} k_{11}(x) & k_{12}(x) \\ k_{21}(y) & k_{22}(y) \end{pmatrix} \right) \quad [3.26]$$

where $\mu_1(x)$ and $\mu_2(y)$ define the mean deformation that moves the point to the most likely X and Y position respectively in the average shape. The 2 x 2 covariance matrix defines how much the position of the point can vary. The components, $k_{11}(x)$ and $k_{22}(y)$ define the variance in the **X** and **Y** directions respectively. The remaining components, $k_{21}(y)$ and $k_{12}(x)$ are used to model how the deformations in the **X** and **Y** directions correlate.

The mean and covariance functions of a Gaussian process can be obtained from example data. The example data may include several shapes in correspondence from which deformations of points in all examples may be observed and an average deformation computed. Similarly, correlations between points may be estimated and used to compute the mean and covariance using the standard formulae for mean and covariance from basic statistics as:

$$\mu(x) = \frac{1}{n} \sum_{i-1}^{n} u^i(x) \quad [3.27]$$

where $u^i(x)$ is the ***i*th** deformation at point **x** and $\mu(x)$ is the average mean deformation for **n** points.

$$k(x, x^i) = \frac{1}{n-1} \sum_{i}^{n} \left(\left(u^i(x) - \mu(x) \right) \left(u^i(x^i) - \mu(x^i) \right) \right)^T \quad [3.28]$$

where $k(x, x^i)$ is the covariance function between any deformations for points ***x*** and ***x*^{i}.**

Gaussian processes allow to define normal models of functions that have been defined using arbitrary discrete data which is a common situation as most data is presented in discrete form for computer implementations (Seeger, 2004).

3.6.3 Posterior probability

A posterior probability gives the probability of event occurring after taking into consideration some new information or data (Webb, 2010). It is usually computed by updating the prior probability by using Bayes' theorem (López et al., 2015).

In the shape modelling context, the posterior probability can be defined using the Bayes theorem as used in probability theory and statistics as:

$$p(u \mid \Gamma_T) = \frac{p(u)\,p(\Gamma_T \mid u)}{p(\Gamma_T)} \qquad [3.29]$$

where $p(u)$ is the prior knowledge, $p(\Gamma_T \mid u)$ is a likelihood function and $p(\Gamma_T)$ is a normalization term. In shape modelling, the prior knowledge is a shape model that gives statistical knowledge about how a shape looks and varies, hence giving probabilistic information about the deformation fields of the shape. The likelihood function is a distance measure that explains how well the solution u explains the data. If u is a deformation field, then the posterior probability would be the probability of the deformation, u given the data.

Posterior probability is used in a range of fields including medicine, finance and economics. It can be used in medical imaging for computation of posterior models from statistical shape models. In this context, a posterior model is the likely appearance of the model based on given parameters or prior information.

3.7 Validation of 3D reconstructed surfaces

3.7.1 Hausdorff distance

The Hausdorff distance measures how far two similar points of a metric space are from each other. Two meshes are considered similar if every point of either mesh is close to the corresponding point in the other mesh. The Hausdorff distance has been used for medical image comparisons and has been reported to be an excellent measure for object matching (Dubuisson and Jain, 1994; Takacs, 1998).

Given corresponding points x and y from two meshes, the distance between the two points can be defined as the Euclidean distance $d(x,y) = \| x - y \|$ and the distance between a point x and a set of points $F = \{f_1, f_2, \ldots\ldots, f_n\}$ is defined as $d(x,F) = \min_{f \in F} \| x - f \|$. Furthermore, the distance between two points $F = \{f_1, f_2, \ldots\ldots, f_n\}$ and $G = \{g_1, g_2, \ldots\ldots, g_n\}$ is given by:

$$d(F,G) = \max_{x \in F} d(x,G) \qquad [3.30]$$

Equation [3.30] gives the Hausdorff distance between points **F** and **G** (Dubuisson and Jain, 1994).

A variation of the Hausdorff distance is the modified Hausdorff distance (Takacs, 1998). The modified Hausdorff distance is more appropriate for object matching as it has the best performance. It takes small values in presence of low levels of noise and takes larger values in presence or higher levels of noise. The modified Hausdorff distance is defined by:

$$d(F,G) = \frac{1}{N_f} \sum_{f \in F} \min_{g \in G} \| f - g \| \qquad [3.31]$$

where N_f gives the total number of points in set **F**, and **f** and **g** are the points in sets **F** and **G** respectively (Takacs, 1998).

3.7.2 Procrustes distance

Procrustes distance is the distance between shapes after they have been superimposed (Al-Aifari et al., 2013). Procrustes aligns shapes and minimises the differences between these shapes to ensure that only true shape differences are defined. The Procrustes distance is approximated as a square root of the sum of the squared differences between the coordinates of points in the two superimposed positions from the same centroid. The squared Procrustes distance between two aligned points $\mathbf{p_1}$ and $\mathbf{p_2}$ is given by:

$$p^2 = \sum_{j=1}^{n} [(x_{j1} - x_{j2})^2 + (y_{j1} - y_{j2})^2] \qquad [3.32]$$

In equation [3.32], **p** is the Procrustes distance, ($\mathbf{x_{j1}}$, $\mathbf{y_{j1}}$) and ($\mathbf{x_{j2}}$, $\mathbf{y_{j2}}$) are the image coordinates of points $\mathbf{p_1}$ and $\mathbf{p_2}$ respectively (Stegmann and Gomez, 2002).

3.7.3 Euclidean distance

Euclidean distance is defined as the distance between two points that are in an Euclidean space (Danielsson, 1980). The Euclidean space is a set for which all distances between all the members of the set are well defined. Euclidean distance can be used to assess how close two corresponding points are. These points can be located on the same object or between two similar objects. On the same object, this distance is called the inter-landmark distance (between points, **r** and **q** or **s** and **p**). Between different objects, the distance is obtained as the Euclidean distance between corresponding points (between points, **s** and **r** or **p** and **q)** (Figure 3.9).

Given two points, **p** and **q** with 3D coordinates (p_1, p_2, p_3) and (q_1, q_2, q_3), the Euclidean distance is given by equation [3.33].

$$ED(p,q) = ED(q,p) = \sqrt{(q_1 - p_1)^2 + (q_2 - p_2)^2 + (q_3 - p_3)^2} \qquad [3.33]$$

where ED is the Euclidean distance between points **p** and **q** (Liberti et al., 2014).

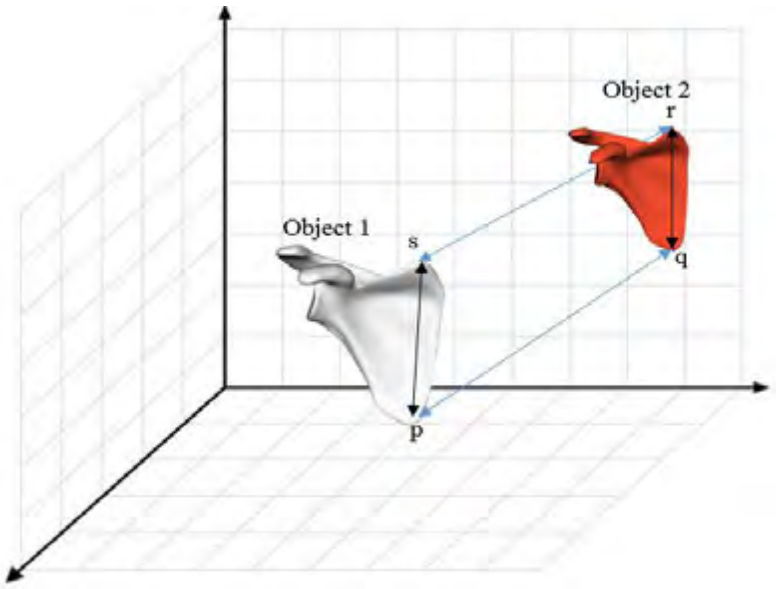

Figure 3.9: Euclidean and inter-landmark distances between points on objects 1 and 2.

3.7.4 Inter-landmark distance

Inter-landmark distance is the linear distance between two landmarks located on the same object. It is widely used in morphometric research to quantitatively analyse the shape, form and size of organisms. Given two points, **p** and **s** with 3D coordinates (p_1, p_2, p_3) and (s_1, s_2, s_3), the inter-landmark distance between points, **p** and **s** can be calculated using equation [3.34].

$$ILD(p,s) = ILD(s,p) = \sqrt{(s_1 - p_1)^2 + (s_2 - p_2)^2 + (s_3 - p_3)^2} \qquad [3.34]$$

In equation [3.34], ILD is the inter-landmark distance between points, p and s. Chimhundu et al. (2014) used the inter-landmark distances of the femur to assess the femoral neck anteversion (Chimhundu et al., 2016).

3.7.5 Average distance

The average distance is the mean of the distances between the closest corresponding points on two models. The average distance is a quantity that defines how large the Euclidean distance between any two points is expected to be defined by:

$$avgdist(X) := \mathrm{E}[\| x - y \|] = \frac{1}{\alpha(X)^2} \int_X \int_X \| x - y \| \, d\alpha(x) d\alpha(y) \qquad [3.35]$$

where α denotes the **s**-dimensional Lebesgue measure (Góra and Boyarsky, 1988), a metric measure assigned to subsets of s-dimensional Euclidean space and **E[||x-y||]** is the Euclidean distance between corresponding points (Burgstaller and Pillichshammer, 2009).

3.8 Summary of the theoretical concepts for landmark-based 3D approximations

In summary, a theoretical framework for landmark-based 3D approximations has been described. This includes the utilization of X-ray stereophotogrammetry, a method used to localize 3D coordinates of points on digital 2D X-ray images (Douglas et al., 2004). A 3D projective transformation by Adams (1981) and modified by Chimhundu et al. (2014) to suit Lodox Statscan geometry has been presented. This method can be used to achieve X-ray stereophotogrammetry on images obtained using the Lodox Statscan system, whose imaging geometry has also been presented.

The presented theoretical framework also includes a landmark reproducibility to determine the reproducible landmarks of the scapula bone (Ohl et al., 2010 ; Schwartz et al., 2011; Borotikar et al., 2015). These landmarks are good candidate points for landmark-constrained shape model fitting since they can reliably be re-selected with minimal errors. This implies that there is a minimal landmarking uncertainty at these landmarks which can potentially result in better 3D approximations.

Finally, the presented landmark-based 3D approximation framework ends with a landmark-constrained shape model fitting process. This stage uses the transformations, Gaussian processes and posterior probability discussed to predict the shape of a model given the landmarks.

The theoretical concepts discussed were explored and used to approximate a patient-specific 3D model of a scapula bone from 2D X-ray images of the shoulder obtained using the Lodox Statscan system. The research approaches used based on this framework are discussed in the chapters to follow.

4 RESEARCH APPROACH: STAGE 1 – X-RAY STEREOPHOTOGRAMMETRY

4.1 Overview

The objective of the first stage was to reconstruct the (***X, Y, Z***) 3D real-world coordinates of any point on a calibrated set of 2D images obtained using Lodox Statscan system. The first stage was the X-ray stereophotogrammetry (Figure 4.1) as shown in the theoretical framework of landmark-based 3D approximations (Figure 3.1).

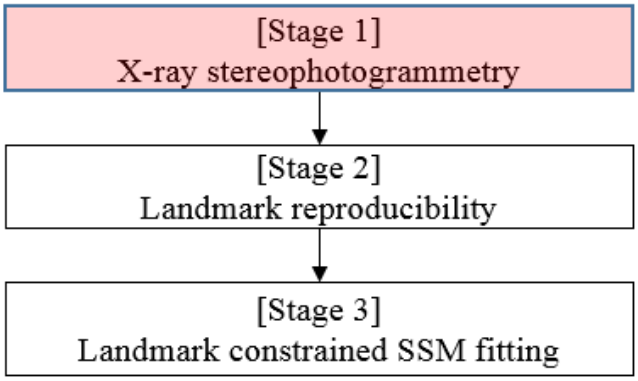

Figure 4.1: The first stage in the research pipeline, X-ray stereophotogrammetry.

An X-ray stereophotogrammetry technique developed by Chimhundu et al. (2014) was utilised (Figure 4.2).

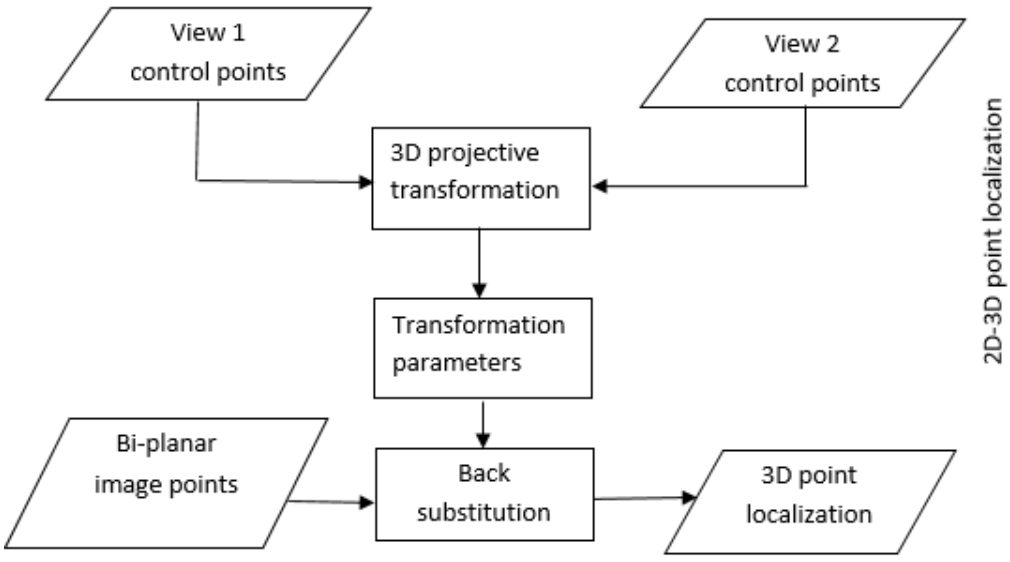

Figure 4.2: The X-ray stereophotogrammetry technique, using two pairs of bi-planar control points and 3D projective transformation to compute the transformation parameters mapping image coordinates to 3D real-world coordinates.

4.2 Control point acquisition

A previously developed rectangular calibration frame (Chimhundu et al,. 2014) (Figure 4.3) containing eight radio-opaque steel bearings 5 mm in diameter with known 3D coordinates was scanned using the Lodox Statscan system. The eight control points are numbered in increasing ***Y*** values along the scan direction (Figure 3.3) of the Lodox Statscan system and there are no points with the same ***Y*** value. This arrangement is desired as it increases the number of control points on the same **X**-axis without weakening the calibration method (Douglas et al., 2004). Eight control points were used because the eight-point algorithm (Chimhundu et al., 2014) used to derive the fundamental matrix (section 3.3.5) requires eight points.

The calibration frame was scanned from two different perspectives with a separation angle of 75° from two different heights with a height difference of 200 mm to obtain four control images (Figure 4.3). The control images were used to calculate the transformation parameters which map the (**u,v**) image points to the (**X,Y,Z**) real-world coordinates. A height difference of 200 mm was used because this was sufficient calibration volume to encompass the torso during shoulder radiography to obtain 2D X-ray images of the scapula, however specific regions of the body such as the hand could use smaller volumes. Although increasing the separation angle between perspectives towards 90° results in less reconstruction errors (Chimhundu et al., 2016), a separation angle of 75° was chosen to maintain visibility of calibration points, which were not visible at 90° due to too much attenuation from the perspex calibration frame at that angle (Chimhundu et al., 2014).

The two sets of images used to calculate the calibration parameters were obtained using the following radiography arrangement.

1. Two views (oblique lateral and AP) taken from the reference height (978 mm from the X-ray source).
2. Similarly two views taken from the final height (1178 mm from the X-ray source).

A graphical user interface (GUI) was designed using Java Abstract Window Toolkit (AWT) (Hemrajani, 1996) and Scala programming language (Odersky et al., 2004) to reconstruct the 3D coordinates of points selected on 2D images. The GUI allows for the control points in each of the two sets of bi-planar control images to be selected to obtain the image coordinates from the reference and final heights.

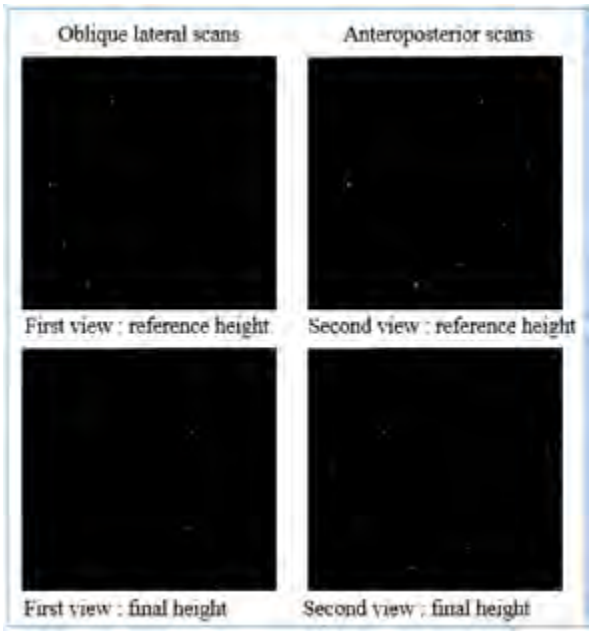

Figure 4.3: The four calibration control images obtained from the bi-planar perspective scans from the reference and final heights.

The mouse-click event was used to track the user clicks in the image panel and using the Window's coordinate system, the clicked point coordinates are stored as an array of points. The Window's coordinate system utilises the pixels as the basic unit of measure hence the stored coordinates are converted into millimetres (mm) for consistency with the reference measurements and saved in the text field (Figure 4.4) selected by the user as the image ***u*** and ***v*** coordinates.

The GUI can automatically compute the centroid of each of the control points as image coordinates. Automatic identification of landmarks is desired as it minimises the human errors introduced by manual landmarking (Subburaj et al., 2009; Palaniswamy et al., 2010). Image analysis techniques were utilised to detect the white clusters on the black background (Figure 4.4) and compute the individual centroids of the clusters. The white pixels in the images were detected using the color.white.getRGB method implemented in Scala programming language which returns the white pixels in a binary image (Chapter, 1999). Connected-component labelling was used to separate the different white clusters (composed of many white pixels), assigning a unique ID to each cluster, and consequently computing its centroid. The connected-component algorithm identifies connected pixels in a binary image and groups them into different clusters (Paralic, 2012). The automatically computed centroid of each cluster is set in the corresponding text fields (highlighted rectangles in Figure 4.4).

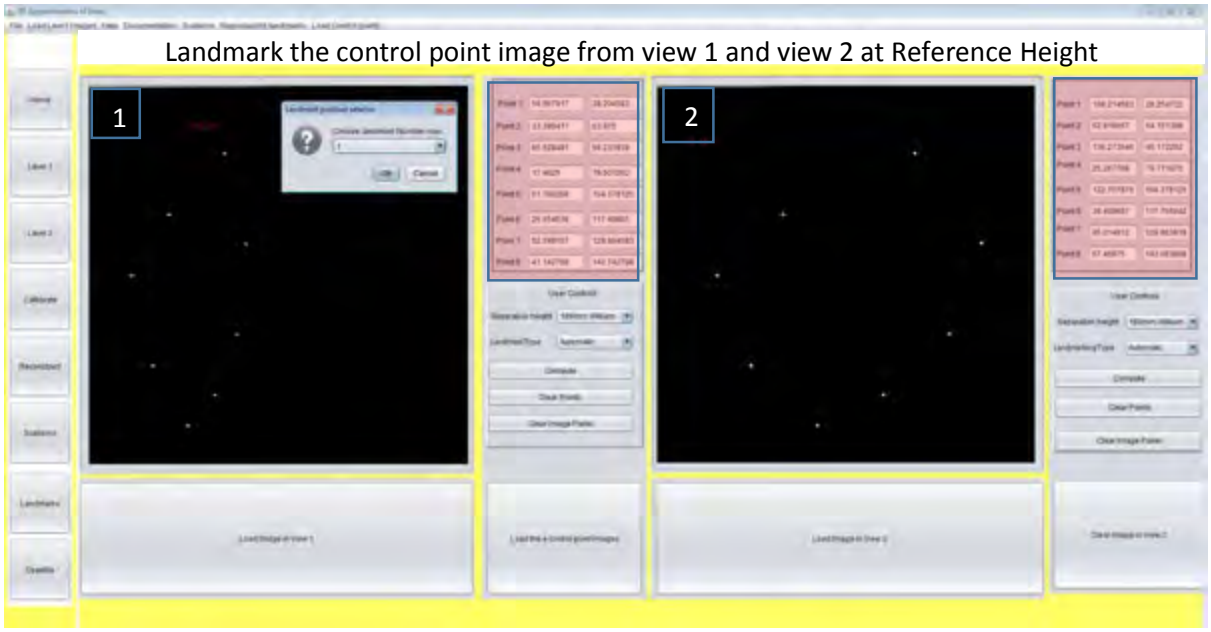

Figure 4.4: GUI for selecting the control image point coordinates (highlighted rectangles) from the first (panel 1) and second (panel 2) views from reference height.

Similarly, the image coordinates of the bi-planar control images obtained from the final height were computed (Figure 4.5).

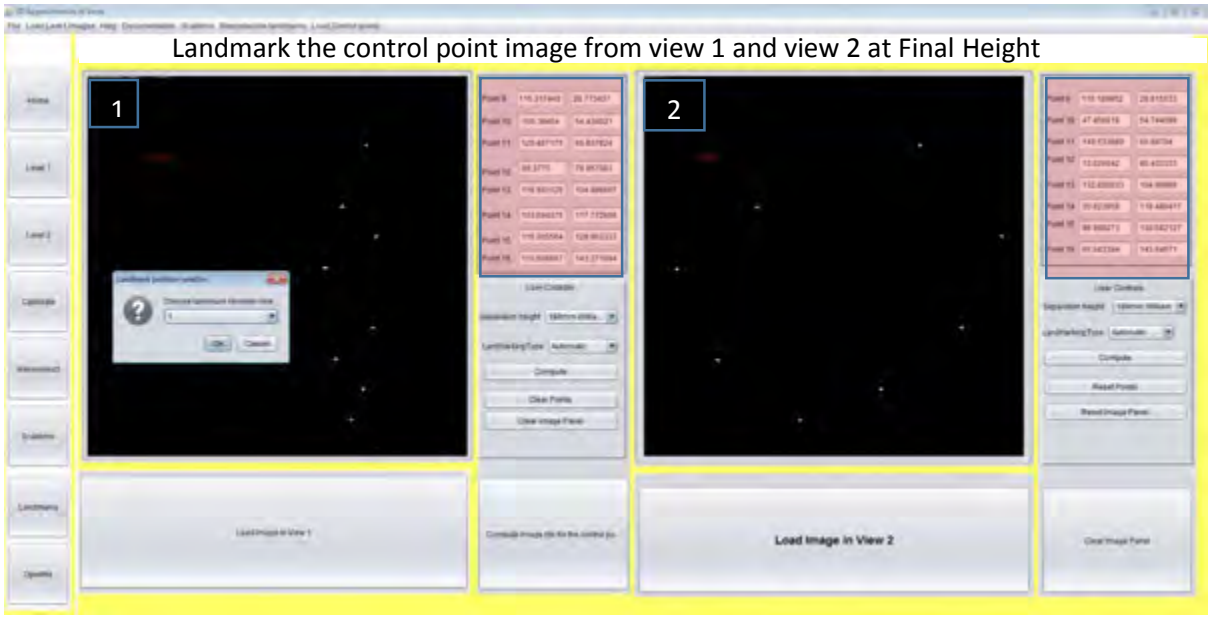

Figure 4.5: GUI for selecting the control image point coordinates (highlighted rectangles) from the first (panel 1) and second (panel 2) views from the final height.

The 32 image coordinates obtained from the four control point images (Figures 4.4 and 4.5) were used to compute the transformation parameters by the utilisation of a 3D projective transformation (section 3.3.2).

4.3 3D projective transformation

A 3D projective transformation was used to establish correspondence between the (**X, Y, Z**) real-world 3D coordinate and the bi-planar (**u, v**) image coordinates for each of the control points. The image coordinates were obtained as described in section 4.2, and the reference **X, Y** and **Z** distances of the control points on the calibration frame were measured manually using a vernier caliper from a defined reference point as the real-world 3D coordinates. The relationship between the image coordinates obtained from Figures 4.4 and 4.5, and the reference real-world 3D coordinates was established using equations [3.4] and [3.5] for the first view and equations [3.6] and [3.7] for the second view respectively. These equations were used to obtain the transformation parameters (section 3.3.3).

4.4 Transformation parameters

The transformation parameters mapping the image coordinates to the real-world 3D coordinates based on the relationship established by the 3D projective transformation in section 4.3, were computed using equations [3.8] – [3.11] for the first view. The underlying algorithm was implemented using a GUI (Figure 4.6) to automatically compute the transformation parameters when the sixteen (***u, v***) image coordinates from each view and the reference 3D coordinates are provided.

Figure 4.6: GUI for computing the transformation parameters using the reference 3D coordinates and the image coordinates.

4.5 3D point reconstruction by back substitution

With transformation parameters obtained from section 4.4, 3D point reconstruction of any 2D point from bi-planar 2D images was achieved through back substitution (section 3.3.4) with

the aid of epipolar geometry (section 3.3.5). Epipolar geometry guides the location of the corresponding point in the second view. The 3D projective transformation equations [3.4] – [3.7] were re-written as a system of linear equations [4.1] – [4.4] respectively (Appendix A).

$$u = p_{11}X + p_{12}Y + p_{13}Z + p_{14} \quad [4.1]$$

$$v = p_{21}X + p_{22}Y + p_{23}Z + p_{24} \quad [4.2]$$

$$u' = p'_{11}X + p'_{12}Y + p'_{13}Z + p'_{14} \quad [4.3]$$

$$v' = p'_{21}X + p'_{22}Y + p'_{23}Z + p'_{24} \quad [4.4]$$

where $\mathbf{p_{11}}=(b_{11}-ub_{21})$, $\mathbf{p_{12}}=(b_{12}-ub_{22})$, $\mathbf{p_{13}}=(b_{13}-ub_{23})$, $\mathbf{p_{14}}=(b_{14})$, $\mathbf{p_{21}}=(b_{31}-vb_{41})$,$\mathbf{p_{22}}=(b_{32}-vb_{42})$, $\mathbf{p_{23}}=(b_{33}-vb_{43})$ and $\mathbf{p_{24}}=(b_{34})$. [4.5]

The values of $\mathbf{b_{ij}}$ are the transformation parameters obtained from section 4.4. Applying back substitution to the above equations yielded the 3D reconstructed coordinates **X, Y** and **Z** given by equation [4.6] (Chimhundu et al., 2014).

$$Y = \frac{(\phi_v\beta_u - \beta_v\phi_u)}{(\beta_u\alpha_v - \beta_v\alpha_u)},\ X = \frac{(u - p_{12}Y - p_{14})}{p_{11}} \text{ and } Z = \frac{(\phi_u - \alpha_u Y)}{\beta_u} \quad [4.6]$$

where

$$\alpha_u = p_{11}p'_{12} - p'_{11}p_{12}, \quad \alpha_v = p_{21}p'_{22} - p'_{21}p_{22}, \quad \beta_u = p_{11}p'_{13} - p'_{11}p_{13}$$

$$,\beta_v = p_{21}p'_{23} - p'_{21}p_{23}, \quad \phi_u = p_{11}u' - p'_{11}u + p'_{11}p_{14} - p_{11}p'_{14}, \quad p_{13} = b_{13} - ub_{23}$$

$$\phi_v = p_{21}v' - p'_{21}v + p'_{21}p_{14} - p_{21}p'_{24}, \quad p_{11} = b_{11} - ub_{21}; \quad p_{12} = b_{12} - ub_{22}; \quad p_{14} = b_{14};$$

$$p_{21} = b_{31} - vb_{41}; \quad p_{22} = b_{32} - vb_{42}; \quad p_{23} = b_{33} - vb_{43}; \quad p_{24} = b_{34}. \quad [4.7]$$

The values of $\mathbf{p_{ij}}$ are obtained from the projection matrices which project 3D to 2D image coordinates calculated from equation [4.5] using the computed transformation parameters.

4.6 Epipolar constraint implementation

Using well-established transformation parameters, the epipolar geometry was implemented using an essential matrix (section 3.3.5) which is a 3 × 3 matrix that relates bi-planar image points in stereo images (Horn, 1990). The following steps were followed to calculate the essential matrix, **E** for the implementation of the epipolar constraint in the developed GUI (Figure 4.7).

1. Projection matrices, **P** and **P′** for the first and second views respectively were calculated using equation [4.8]. A projection matrix is a 3 × 4 matrix which projects a 3D point to a 2D image (Chimhundu et al., 2014).

$$\mathbf{P}=\begin{bmatrix} b11 & b12 & b13 & b14 \\ b31 & b32 & b33 & b34 \\ 0 & 0 & 0 & 1 \end{bmatrix} \text{ and } \mathbf{P'}=\begin{bmatrix} b^1 11 & b^1 12 & b^1 13 & b^1 14 \\ b^1 31 & b^1 32 & b^1 33 & b^1 34 \\ 0 & 0 & 0 & 1 \end{bmatrix} \quad [4.8]$$

where $\mathbf{b_{ij}}$ and $\mathbf{b^i_{ij}}$ are the transformation parameters for the first and second view, respectively.

2. A null vector, $\mathbf{P_{null}}$ of projection matrix, **P** was computed using the singular value decomposition (SVD) and least squares solution (Golub and Reinsch, 1970). This vector represents a vector orthogonal to all rows in matrix, **P**.
3. A skew symmetric matrix, **S** was calculated using equation [3.17].
4. The essential matrix, **E** relating the image coordinates in the two views was calculated using equation [3.16].
5. The epipolar line, ***epi*** in the second view of an image point, **K** from the first view is given by **E* K**. The matrix, ***epi*** which defines the epipolar line, is a 3 x 1 matrix with entries **A, B** and **C** being the first, second and third elements of this matrix. These entries are used to draw a straight line in the second view using the equation of a straight line, **A**X + **B**Y + **C**=0 (Burns et al., 1986).
6. Finally the epipolar line, ***epinv*** in the first view of an image point, **L** from second view is given by **Einv * L**; where ***Einv*** is the inverse of the essential matrix, **E** and **L** is the image coordinate of point **L**.

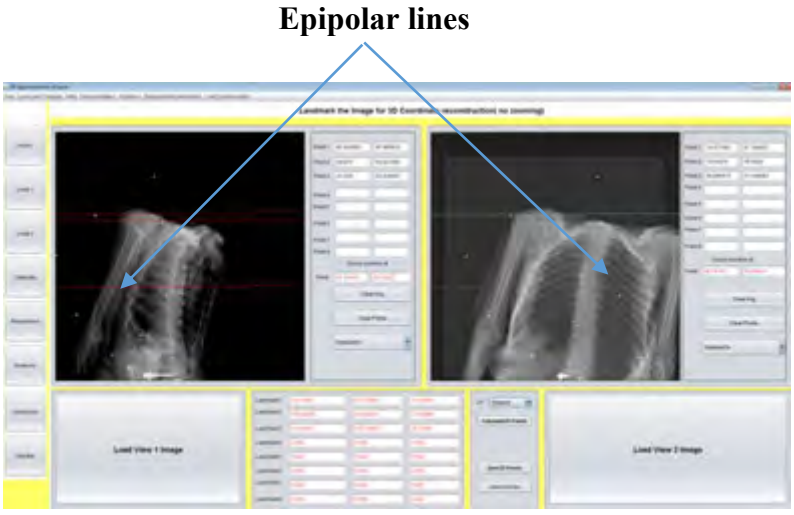

Figure 4.7: GUI for 3D point localization using the computed transformation parameters and the epipolar geometry.

4.7 Conclusion

A 3D point localization tool was developed using Java Abstract window toolkit and Scala programing language based on the mathematical algorithms developed by Chimhundu et al. (2014).

Increasing the image separation angle of the bi-planar images to 75° has potential to reduce the reconstruction errors (Chimhundu et al., 2014), however it compromises on the ease of selecting the corresponding point in the second view which may be partially solved by the use of epipolar geometry. The epipolar geometry is very important because reducing the errors in the corresponding point reduces the resultant reconstruction error in the 3D coordinates. During the calculation of the transformation parameters (section 4.2), the metallic landmarks on control point images were easy to select without an epipolar line due to their proper visibility (Figures 4.5 and 4.6). However, it was difficult to select the corresponding landmarks on the scapula image in the second view without the help of an epipolar line (Figure 4.7). The difficulty in selecting a corresponding point increased even further, if many close points were required (Figure 7.15).

The developed tool is suitable for 3D point reconstruction for applications like cephalometry (Douglas, 2004), measurement of inter-landmark distances (Chimhundu et al., 2014) and spinal shape assessment (Rapała et al., 2009). The tool is also useful for landmark-constrained SSM fitting, further discussed in chapter 7.

Chapter 5 describes experiments done to validate the tool in 3D reconstruction of landmarks.

5 3D LOCALIZATION VALIDATION

5.1 Overview

Validation of the three-dimensional localization was the last step of X-ray stereophotogrammetry (the first stage of the reconstruction pipeline). 3D localization validation included a set of experiments to validate the developed 3D localization tool. These experiments included control and test point reconstruction tests (section 3.4) and assessing the consistency of the measurements from the tool by different observers (inter-observer).

5.1.1 Experiment 1: Control point reconstruction

The first experiment aimed to assess the mathematical correctness of the 2D-3D reconstruction algorithm. The images used in the calculation of the transformation parameters were used to compute the known 3D coordinates of the eight control points. Two observers selected the control points and reconstructed the 3D coordinates of the selected points using the developed tool (Figure 4.7) for two trials each. The average value of **X**, **Y** and **Z** of each of the four sets of the 3D reconstructed coordinates was computed (Appendix B)

The reconstruction errors (e_x, e_y, e_z) (Table 5.1) in the **X, Y** and **Z** coordinates respectively between the reconstructed coordinates and the reference coordinates were calculated using equations [3.18] – [3.20] respectively. The resultant reconstruction error, $\mathbf{E_i}$ for the $\mathbf{i^{th}}$ landmark was calculated using equation [3.21].

Average reconstruction errors of 0.14 mm, 0.07 mm, 0.04 mm and 0.19 mm for $\mathbf{e_x}$, $\mathbf{e_y}$, $\mathbf{e_z}$ and $\mathbf{E_i}$ respectively were obtained.

Table 5.1: The average reconstruction errors e_x, e_y, and e_z from control point reconstruction

Landmark	e_x(mm)	e_y(mm)	e_z(mm)	Ei(mm)
1	0.15	0.12	0.06	0.20
2	0.12	0.11	0.09	0.18
3	0.46	0.29	0.01	0.54
4	0.02	0.00	0.13	0.13
5	0.12	0.02	0.00	0.12
6	0.01	0.01	0.06	0.06
7	0.08	0.06	0.00	0.10
8	0.21	0.01	0.01	0.21

5.1.2 Experiment 2: Test point reconstruction

The second experiment aimed to assess the accuracy of test points (ie points with known 3D coordinates but not used in the calculation of the transformation parameters). Using the developed 3D localization tool, the 3D coordinates of seven landmarks selected on a 2D image of a dry pelvis (test image) were reconstructed. The reconstructed 3D coordinates were compared with the measurements obtained using method designed by Chimhundu et al. (2014). Similarly to experiment 1, two observers selected the landmarks on the test images and reconstructed the 3D coordinates of the selected landmarks for two trials each. The average **X**, **Y** and **Z** value of the four sets of the 3D reconstructed coordinates was computed (Appendix B).

Since the two sets of measurements under comparison were obtained from different coordinate systems, inter-landmark distances (ILD) (section 3.7.4) between points were compared using equation [3.34]. The inter-landmark distances between the points obtained by Chimhundu et al. (2014) and the reconstructed measurements are represented by $\mathbf{ILD^1}$ and $\mathbf{ILD^2}$ respectively. The absolute error, **E** was calculated as the absolute difference of $\mathbf{ILD^1}$ and $\mathbf{ILD^2}$. The values of $\mathbf{ILD^i}$ are the Euclidean distances between landmarks **1** and **2**, **2** and **3, 3** and **4**, **4** and **5**, **5** and **6**, **6** and 7 and finally between **7** and **8** (Table 5.2).

An average error **E** of 0.34 mm between the inter-landmark distances from the measurements obtained by the method developed by Chimhundu et al. (2014) and the reconstructed measurements was obtained.

Table 5.2: The absolute error, E, between inter-landmark distances of a dry pelvis, by Chimhundu et al. (2014) ($\mathbf{ILD^1}$) and the developed 3D localization tool ($\mathbf{ILD^2}$).

Landmark	$\mathbf{ILD^1}$ (mm)	$\mathbf{ILD^2}$ (mm)	E (mm)
1	202.05	202.76	0.71
2	153.91	153.63	0.28
3	38.71	39.47	0.76
4	94.51	94.47	0.04
5	183.79	183.39	0.40
6	237.35	237.20	0.15
7	76.49	76.53	0.04

5.1.3 Experiment 3: Inter-observer reliability

The third experiment was to investigate the consistency of the reconstructed 3D coordinates (measurements) taken by different observers, using the developed tool. The reconstructed 3D coordinates from the two observers in experiment two (test point reconstruction) were used for this assessment as test point reconstruction is a true test of system consistency (Douglas et al., 2004). For each reconstructed **X, Y** and **Z** coordinate, the reference position was given by the average position of the four measurements. The observed maximal differences and average measurements were computed from this reference position. The error between the observers using this technique is given by the root-mean square (rms).

$$rms = \sqrt{\sum_{i=1}^{n} SD_i^2} / n \qquad [5.9]$$

In equation [5.9], **n** is the total population and SD_i is the standard deviation for the **ith** subject. Ohl et al. (2010) used this technique to investigate the reproducibility of shoulder bony landmarks. For a normal distribution, 95% confidence interval (CI) is equal to 2*rms (Gluer et al., 1995). A Two Way Analysis of Variance (ANOVA) was used to assess if there is any relationship between the two measurements from the different observers. Significance was set to $\boldsymbol{p} < 0.05$ (Rousseau et al., 2007). The intraclass correlation coefficient (ICC) was used to quantify the degree to which the different observers agreed (inter-observer reliability) (Cook, 2000). The Statistical Package for the Social Sciences (**SPSS**) was used to compute the ICC.

The results of the inter-observer experiments (Appendix B) were described with the average and maximum inter-observer differences, inter-observer ***p*** value and the 95% CI (Table 5.3). The inter-observer ***p*** value was used to determine if any of the differences between the observers are statistically significant (Goodman, 2008).

Table 5.3: Results from the inter-observer reliability assessment

No.	Point	Average interobserver difference	Maximum inter-observer difference	Inter-observer *p* value	95% CI	*p* value of observer 1	*p* value of observer 2
1	**x**	0.05	0.05	0.51	0.41	0.43	0.49
	y	0.05	0.06	0.34	0.52	0.28	0.32
	z	0.01	0.02	0.09	1.10	0.07	0.07
2	**x**	0.04	0.04	0.41	0.30	0.60	0.30
	y	0.30	0.32	0.18	0.42	0.07	0.21
	z	0.02	0.01	0.32	1.90	0.11	0.13
3	**x**	0.09	0.09	0.60	0.49	0.80	0.76
	y	0.29	0.30	0.81	0.48	0.56	0.48
	z	0.05	0.09	0.08	0.98	0.13	0.16

There were no significant differences found to result from the observers (Table 5.3). Overall, the ICCs for the **X**, **Y** and **Z** coordinates between the observers were excellent (> 0.93).

5.2 Discussion of 3D localization validation

5.2.1 Control point reconstruction

Control point reconstruction was used to check the mathematical correctness of the reconstruction algorithm before test point reconstruction. However, it is not considered a true test of system accuracy (Challis and Kerwin, 1992). This is because the points used in the system testing are also used for system calibration.

Since both the 2D and 3D coordinates of the control points are used in the computation of calibration parameters, no errors are expected in an error free system. However in real systems, factors like noise, decimal place truncation and differences in matrix packages used, often result in the 3D coordinates not being exactly reproducible and this accounts for the observed reconstruction errors.

Average reconstruction errors (0.14 mm, 0.07 mm, and 0.04 mm) were obtained in the **X**, **Y** and **Z** coordinates. These values were considered to be acceptable, as they were comparable with errors reported in previous studies. Work on 3D point localization in low-dose X-ray images (Douglas et al., 2004) yielded (X, Y, Z) coordinate reconstruction errors of (0.25,0.42,0.37) mm respectively, while work by Chimhundu et al. (2014) yielded (X, Y, Z) average reconstruction errors of (0.08, 0.04, 0.06) respectively.

5.2.2 Test point reconstruction

Since the pelvis images used in this test were not used in the computation of the transformation parameters, these images are a suitable candidate for the assessment of the accuracy of the system.

An average difference of 0.34 mm between inter-landmark distances obtained from the method developed by Chimhundu et al. (2014) and the developed 3D localization tool showed that the 3D space coordinates of any landmark from the two systems are comparable. Overall ICC of > 0.93 indicated that the **X, Y** and **Z** reconstructed coordinates from the two observers have a very high level of agreement.

5.3 Conclusion of landmark localization

A 3D point localization tool described in Chapter 4 was validated. Control point reconstruction (Table 5.1) and test point reconstruction (Table 5.2) confirm that measurements from the new tool are acceptable.

6 RESEARCH APPROACH: STAGE 2 - LANDMARK REPRODUCIBILITY

6.1 Overview

The second stage in the research pipeline (Figure 3.1) was the landmark reproducibility (Figure 6.1). It was sub-divided into three sub-problems: 1) Determining the reproducible landmarks of the scapula image and model, 2) Shoulder radiography on Lodox Statscan system to obtain bi-planar 2D X-ray images of the scapula, and finally 3) Determining landmarking error and uncertainty on the 2D X-ray images. These sub-problems are discussed in the sections to follow.

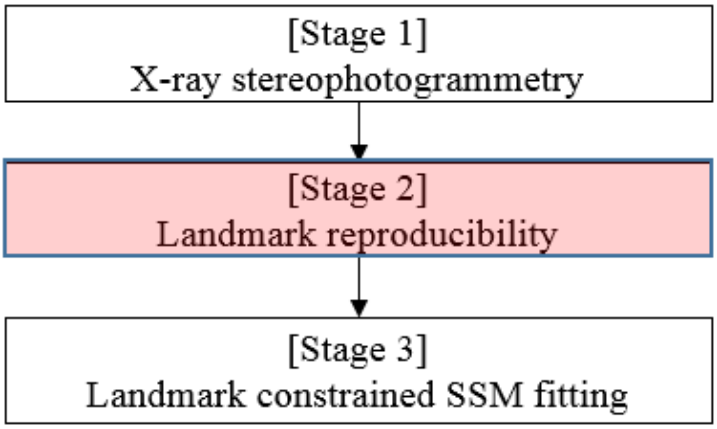

Figure 6.1: The second stage in the research pipeline. Landmark reproducibility (highlighted rectangle) focusses on assessing the landmarks of the scapula that are reproducible, obtaining shoulder radiographic images from Lodox Statscan and evaluating landmarking errors and uncertainty on 2D X-ray images.

6.2 Reproducible landmarks

The reproducible landmarks (section 3.5) considered for this research are those reported by the studies on locating shoulder bony landmarks by Ohl et al. (2010) and on clinical validation and reliability of landmark selection of an anatomically augmented SSM of the scapula by Borotikar et al. (2015) (Table 6.1).

The supra glenoid rim, infra glenoid rim, superior angle, inferior angle, coracoid process, acromion, base of scapula spine and the scapula notch as reported by the two studies were considered as the universal set of the reproducible landmarks from which the eligible landmarks (Figure 6.3) for this research were selected. Eligible landmarks for this project are those that could clearly be identified from the AP and oblique lateral view scans during shoulder radiography on Lodox Statscan system.

Table 6.1: Results from the studies by Ohl et al. (2010) and Borotikar et al. (2015) on reproducible landmarks of the scapula.

STUDY	REPRODUCIBLE LANDMARKS	REPRODUCIBILITY (CI = 95% confidence interval)
Ohl et al. (2010)	Tip of Coracoid process	CI<2.13 mm
	Inferior Glenoid rim	CI<2.91 mm
	Acromion	CI<2.72 mm
	Lateral border	CI<3.67 mm
Borotikar et al. (2015)	Borders of the scapula	Intra- and inter-observer reliability > 70%
	Areas around Glenoid rim	Intra- and inter-observer reliability > 80%

6.3 Shoulder radiography on Lodox Statscan system

Shoulder radiography was performed using standard protocols for this purpose (Sanders and Jersey, 2005). However to expose the scapula, modifications were made onto these protocols to expose the reproducible landmarks in the AP and lateral views.

A cadaveric shoulder was placed at one extreme end of the scanning table of the Lodox Statscan system. The table was set at the 1178 mm from the X-ray source. An AP (0^0) and an oblique lateral (75^0) view of the shoulder were taken from this height to obtain bi-planar 2D X-ray images (Figure 6.2).

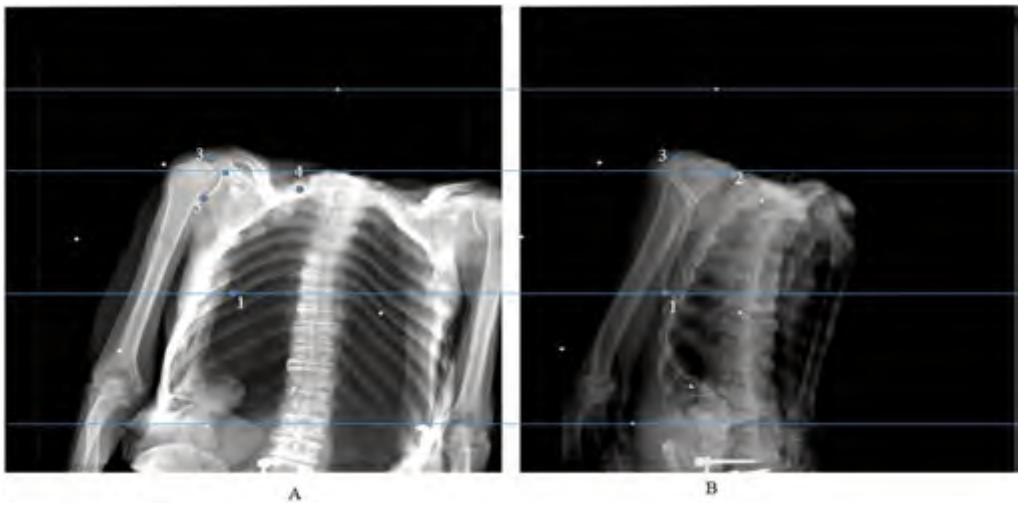

Figure 6.2: (A) AP and (B) Oblique lateral shoulder radiography. (1) Inferior angle, (2) Coracoid process, (3) Acromion (4) Superior angle and (5) Infra glenoid rim

The limitation of the adopted radiography protocol was that only a few of the reproducible landmarks could be obtained in the oblique lateral view. Different contrast levels were applied on the acquired 2D X-ray images (Figure 6.2) using Lodox Statscan's Digital Viewing System (DVS) software (Lodox Systems, South Africa) to be able to view the landmarks of interest clearly. This helped to reduce the chances of selecting an incorrect corresponding point on the image in the second view as this would introduce errors in the reconstructed 3D coordinates of the selected landmarks.

A union of the reproducible landmarks reported by Ohl et al. (2010) and Borotikar et al. (2015) was analysed and the common landmarks reported from both studies were identified. The studies showed good reproducibility for the tip of the coracoid process, areas around the tip of the acromion, areas around the glenoid rim and landmarks around the borders of the scapula (Table 6.2).

Table 6.2: Selected scapula landmarks for this research based on results in Table 6.1

STUDY	*INTERSECTING LANDMARKS*	*SELECTED LANDMARKS*
Ohl et al. (2010)	Acromion	Tip of coracoid process
	Coracoid process	Acromion
	Areas around glenoid rim	Inferior Glenoid rim
	Borders of the scapula	Superior Glenoid rim
Borotikar et al. (2015)		Medial border (Root of the scapula spine)
		Inferior angle
		Superior angle
		Scapula notch

Out of the eight reproducible landmarks reported by Ohl et al. (2010) and Borotikar et al. (2015), only three landmarks could clearly be simultaneously selected from the AP and oblique lateral views using the designed 3D point localization tool with the help of the epipolar geometry. These landmarks are the inferior angle, the coracoid process and the acromion (Figure 6.3), hence these are the landmarks that were used as the target points for landmark constrained SSM fitting process, discussed in chapter 7.

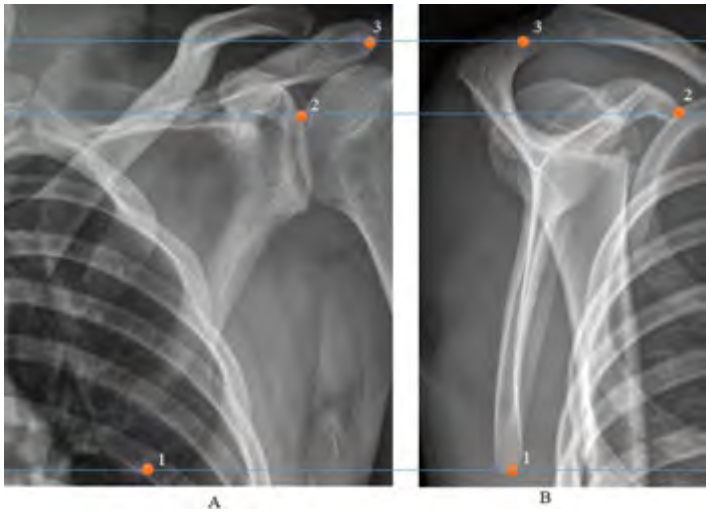

Figure 6.3: Selected reproducible landmarks of the scapula. (A) AP and (B) Oblique lateral shoulder radiography. (1) Inferior angle, (2) Coracoid process and (3) Acromion.

6.4 Landmark localization errors on 2D X-ray images

In X-ray stereophotogrammetry, accurate selection of corresponding landmarks in both perspectives is necessary. This is because the resulting reconstruction error in the reconstructed 3D coordinates is dependent on the accuracy of the landmarking process on the 2D X-ray images. To minimize the possible sources of errors the following constraints were implemented.

1. The corresponding image point in the alternative view lies on the constructed epipolar line to limit the search to only one dimension using epipolar geometry.
2. Landmarking errors were incorporated into the selected landmark as described in section 6.4.1 to control the accuracy of the 3D reconstructed coordinates.

Three-dimensional point localization was based on a set of corresponding anatomical landmarks on 2D X-ray images selected from two views. An approach was developed to take into account the localization errors during the 2D image landmarking and thus control the effect of this error on the reconstructed points, based on prior knowledge about the localization errors.

Different values of the **X** coordinate could easily be selected for the same landmark because the anatomical landmarks selected on the scapula are not provided as sharp edge points. For example, the **Y** coordinate of the acromion could easily be located on the epipolar line, however the **X** coordinate could take on a range of values (Figure 6.4).

Figure 6.4: Landmarking uncertainty on a scapula's curved landmark, the acromion.

Experiments were carried out to determine the landmarking error and uncertainty on the three selected landmarks on the 2D X-ray images. Error is the difference between a measurement and a true value (Fitzmaurice, 2002). Uncertainty is a measure used to show the range of values within which the true value is asserted to lie (Borgonovo, 2007). The experiments to assess the landmarking errors and uncertainty are discussed in the sections to follow.

6.4.1 Experiment 1: Landmarking error on 2D bi-planar X-ray images

The first experiment aimed to determine the landmarking error on 2D bi-planar X-ray images and the resultant reconstruction error in the 3D coordinates. A professional radiographer was consulted to identify the three selected landmarks (Figure 6.3) using the developed tool for a total of five attempts. A time delay of 24 hours was allowed between the attempts to avoid bias during landmarking. The average values of **(u, v)** and **(u^i, v^i)** image coordinates for each landmark from the first and second view respectively were obtained (Appendix C) and used to compute the landmarking error for each landmark. Furthermore, the average values of **u, v** and **u^i, v^i** image coordinates were used to reconstruct the ground truth real world 3D coordinates of the three selected landmarks (the inferior angle, coracoid process and the acromion). The landmarking error for each point was calculated using equations [3.18] – [3.20] and the resultant reconstruction error in the 3D coordinate was calculated using equation [3.21].

Average values of (45.86, 98.17, 75.70 and 98.78) mm for **(u, v**, **u^i** and **v^i)** respectively were obtained. Reconstructed **X, Y Z** 3D coordinates of (180.00, 274.92, 10.90) mm, (159.93,

110.95, 66.17) mm and (140.19, 85.25, 26.31) mm were obtained for the inferior angle, coracoid process and the acromion respectively.

Two-dimensional landmarking errors of (0.56, 0.30, 0.74, and 0.11) mm were obtained for the **u, v**, $\mathbf{u^i}$ and $\mathbf{v^i}$ coordinates respectively and the resultant reconstruction error of 0.64 mm in the 3D coordinates was obtained.

6.4.2 Experiment 2: Landmarking uncertainty on the 2D bi-planar images

The second experiment aimed to determine the landmarking uncertainty on 2D bi-planar X-ray images. The method and results from experiment 1 were used. The landmarking uncertainty in the 2D landmarks was calculated as the average standard deviation of the **u, v** and $\mathbf{u^i}$, $\mathbf{v^i}$ from the obtained average values for each landmark using equation [6.1].

$$SD = \sqrt{\frac{\sum_{i=1}^{n}\left(x_i - \bar{x}\right)^2}{(n-1)}} \qquad [6.1]$$

where $\mathbf{x_i}$ is the $\mathbf{i^{th}}$ measurement and $\bar{x}$ is the mean of **n** measurements considered.

A standard deviation of ± 0.81 mm and a 2D landmarking uncertainty of (45.86 ± 0.81, 98.17 ± 0.81, 75.70 ± 0.81 and 98.78 ± 0.81), at a level of confidence of 95% on the 2D X-ray images was obtained.

6.5 Discussion of 2D landmarking error

Two-dimensional landmarking errors were slightly higher in the (**u** and $\mathbf{u^i}$) than in the (**v** and $\mathbf{v^i}$) image points which are in the **X** and **Y** directions respectively. This is attributed to Lodox Statscan's imaging fan geometry where the beam spreads out more in the **X**-direction (trolley width of Figure 3.3) than in the Y-direction (Irving et al., 2008) . Furthermore, landmarking in the **Y**-direction is guided by the epipolar geometry hence we have priori knowledge of the expected location of a point as it lies on an epipolar line (Chimhundu et al., 2014). This also explains the least landmarking error in $\mathbf{v^i}$, the image point in the **Y**-direction of the second view.

6.6 General discussion and conclusion of landmark reproducibility

During shoulder radiography, the shoulder was placed on the lower scan height such that the scapula bone was within the calibrated volume and within the metallic landmarks (white points) on the calibration frame (Figure 6.2). This ensures accurate 3D reconstructions of any landmark on the scapula that is within the calibrated volume (Douglas et al., 2004). However

a smaller height and a calibration frame could be used for smaller body parts like a finger and dry bones.

Three landmarks were able to provide an approximation of a patient-specific 3D model from a SSM using landmark-constrained SSM fitting as any number of landmarks may be enough to produce a constrained model. The constraining is variant to number of landmarks used and the more we have in anatomically relevant areas the better an approximation in those areas. However, what is anatomically relevant is application dependent and subjective. The calculation of landmarking uncertainty is useful in the landmark-constrained fitting where an indication of the uncertainty in the landmarking is required during the computation of posterior models (section 7.3.5).

7 RESEARCH APPROACH: STAGE 3 - LANDMARK-CONSTRAINED SSM FITTING

7.1 Overview

The last stage in the research protocol (Figure 3.1) was approximating a patient-specific 3D model of a scapula from 2D X-ray images using landmark-constrained SSM fitting (Figure 7.1). It was sub-divided into two sub-problems; 1) the fitting process which produces 3D patient-specific approximation, from 3D coordinates obtained from the reproducible landmarks; and 2) validation of the approximated 3D model.

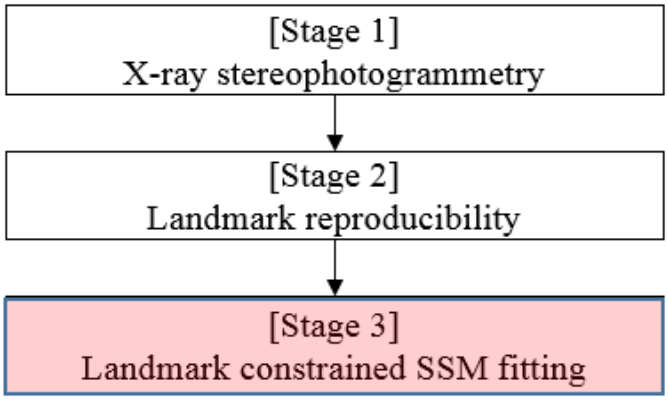

Figure 7.1: The last stage in the research pipeline: Landmark-constrained SSM fitting that produces approximations of patient-specific 3D models from a few landmarks.

7.2 Development environment

The Scalismo interactive fitting developmental framework (Figure 7.2) was used for the fitting process. Scalismo is an open source shape modelling platform developed at the University of Basel, Switzerland. Scalismo makes use of Scalable language (Scala) and runs on Java Virtual Machine (JVM) hence it is platform independent and interoperable with Java programming language. Scala Integrated Development Environment 4.0 was used for the development process.

The hardware requirements for the development environment include a computer running Microsoft Windows, Macintosh or Linux operating system with a minimum memory of 2 GB and processor speed of 2 GHz. However, utilisation of a high computing system with a graphics processing unit (GPU), 32 GB of memory and processor speed of 3.6 GHz increased the processing and execution time by 84% due to the GPU's capability to rapidly manipulate and alter memory for image processing.

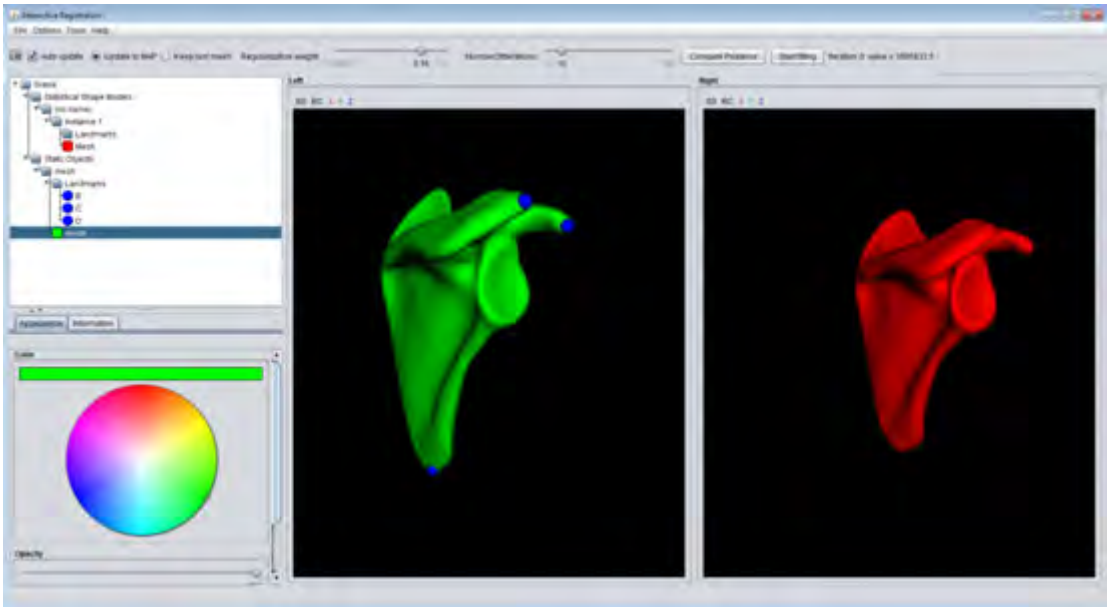

Figure 7.2: The Scalismo interactive fitting developmental framework used for implementation of the landmark-constrained SSM fitting algorithm (University of Basel, Switzerland).

7.3 The fitting process

The fitting process (Figure 7.3) involved deforming a SSM onto the reconstructed 3D coordinates from 2D X-ray images. In the developed framework, the fitting algorithm includes a rigid transform (section 3.6.1) based on a closed form solution (Umeyama, 1991) that transforms the model landmark coordinates into the same coordinate space as the image coordinates. Subsequently a posterior model of the SSM which represents the possible shape variation, given the landmarks was computed using marginal Gaussian processes (section 3.6.2). The sub-stages are discussed in the sections to follow.

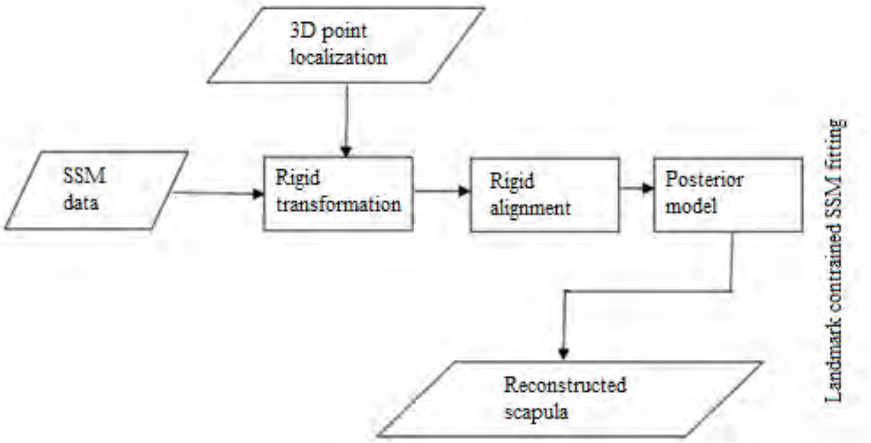

Figure 7.3: Steps of the patient-specific 3D model approximation from a SSM and reconstructed 3D coordinates from 2D X-ray images.

7.3.1 3D point localization

Three-dimensional point localization involved importing the reconstructed 3D coordinates file into the Scalismo platform. The Scalismo implementation of reading 3D landmarks files was used to read the file containing the 3D reconstructed coordinates. The landmarks were added to the SSM data in the Scalismo user interface using the **add landmarks** method implemented in Scalismo that allows for the adding of landmarks to an object in Scalismo scene (Figure 7.2).

7.3.2 SSM data

The scapula SSM (Figure 7.4) used was created from a training dataset of 84 scapulae instances. This is an advance on the successful development and validation of scapula model by Mutsvangwa et al., (2015) which had fewer (21) scapulae instances. Increasing the number of scapulae in the training dataset results in a more flexible SSM (Mutsvangwa et al., 2015).

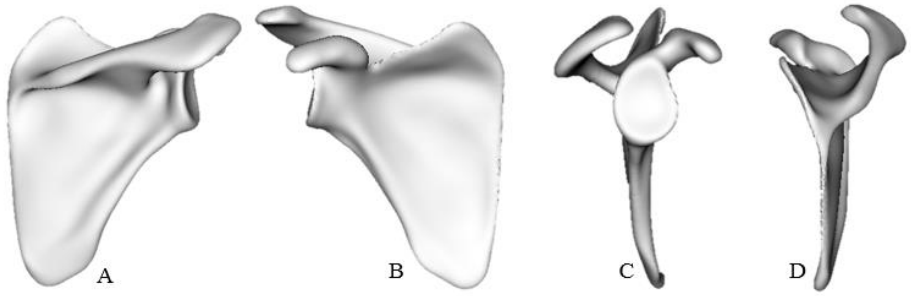

Figure 7.4: The original SSM of the Scapula from which a patient-specific SSM instance was approximated. (A) Posterior, (B) Anterior, (C) Lateral, and (D) Medial views.

7.3.3 Rigid transformation

The reconstructed 3D coordinates and the SSM landmark coordinates were obtained from different coordinate systems, the Windows coordinate system and the Left, Posterior, Superior (LPS) coordinate system respectively. To load the two sets of coordinates in the same 3D space of the Scalismo platform, a transformation was computed that translates the reference (SSM) into the target (reconstructed 3D image coordinates) coordinate system. A transformation, **T(v)** was computed such that:

$$\boldsymbol{M_c} + \boldsymbol{T(v)} = \boldsymbol{I_{0c}} \qquad [7.1]$$

In equation [7.1], $\boldsymbol{M_c}$ is the centroid of the mean SSM obtained by computing the average point of the number of points in the mean SSM, $\boldsymbol{I_{0c}}$ is the centroid of the reconstructed 3D image coordinates (**X, Y, Z**) given by average (**X**), average (**Y**), average (*Z*), *and* $\boldsymbol{T(v)}$ is the transformation that translates the reference landmarks into the target coordinate system. As

discussed in section 3.6.1, a rigid transformation was carried out to remove translations that arise as a result of differences in coordinate systems. The effect of the translations is illustrated in Figure 7.5. The SSM landmarks (black points) are not in the same coordinate system as the 3D reconstructed landmarks (blue points) hence proper alignment may not be achieved to give true point-to-point correspondences.

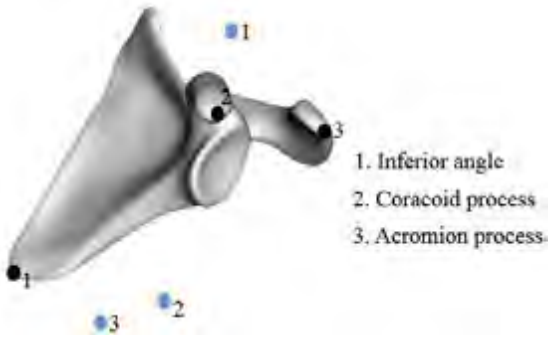

Figure 7.5: Translation effect on the SSM's orientation due to differences in the coordinate systems between the reference (black points) and target (blue points) landmarks

The outcome of the application of transformation, ***T(v)*** obtained from Equation [7.1] to the SSM was a translated SSM (Figure 7.6). The translated model was now in the same coordinate system as the reconstructed 3D coordinates, but not yet aligned. This makes it possible to establish point-to-point correspondences between the translated SSM and the reconstructed 3D coordinates during the alignment stage.

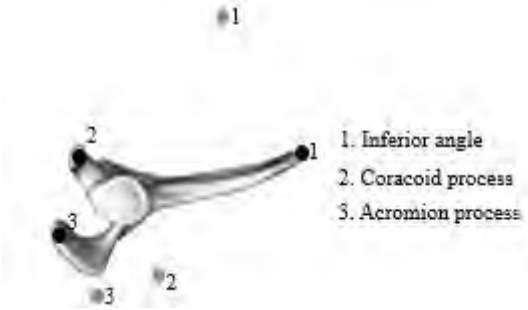

Figure 7.6: A translated SSM after application of a rigid transformation removing the translational effect. Reference (black points) and target (blue point) landmarks.

7.3.4 Rigid alignment

Rigid alignment included the computation of a best transformation mapping a set of reference landmarks on the SSM to the corresponding set of target landmarks. This required the establishment of correspondences between the target and reference landmarks. Rigid alignment was achieved through the following steps.

1. Candidate landmark correspondences were established between the target and reference landmarks. This was achieved by mapping the reference landmark point IDs to the corresponding target landmark point IDs (Table 7.1).
2. Based on the established candidate landmark correspondences, a best transformation was computed. This is a rigid transformation that aligns the two shapes removing the effects of rotation without affecting the shape and size of the images. This was implemented using the **rigid3DLandmarkRegistration** method of Scalismo. The rigid3DLandmarkRegistration method returns a rigid transformation mapping the reference landmarks to the target landmarks.

Table 7.1: Correspondence between target and reference landmark IDs.

	Target landmarks		Reference landmarks	
Landmark	**ID**	**Point**	**ID**	**Point**
Inferior angle	1	(x_t, y_t, z_t)	1	(x_r, y_r, z_r)
Coracoid process	2	(x_t, y_t, z_t)	2	(x_r, y_r, z_r)
Acromion	3	(x_t, y_t, z_t)	3	(x_r, y_r, z_r)

Three landmarks were selected from the target (reconstructed 3D coordinates) and the same landmarks selected from the reference (SSM). These were then mapped together using the corresponding point IDs. This was implemented using the **map** method in Scalismo that maps a pair of corresponding point IDs.

Application of a rigid alignment to the target landmarks and the translated SSM resulted in an aligned model (Figure 7.7) that was necessary for the subsequent fitting process. However the alignment was not sufficiently constrained due to the lower (3) number of landmarks used to establish the landmark correspondences (Table 7.1).

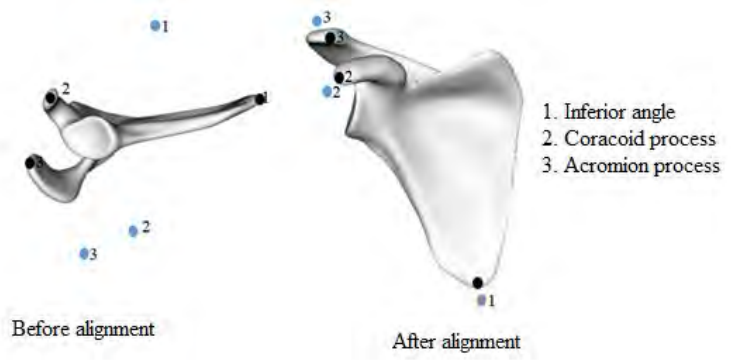

Figure 7.7: Reference (black points) and target (blue points) during alignment.

7.3.5 Posterior model

The posterior model (section 3.6.3) was computed using the ***posterior*** method implementation of Scalismo. The posterior method computes a posterior distribution of the SSM given some sample data (Figure 7.8). The computation of the posterior model required indicating for every correspondence, an uncertainty distribution indicating where the corresponding point can possibly lie. The landmarking uncertainty obtained from section 6.4.2 was included in this uncertainty distribution.

Figure 7.8: Some of random instances (red) obtained from the posterior distribution. These instances are constrained at the selected three landmarks (black points), but with more variations in other regions.

7.3.6 Reconstructed scapula

The mean of the posterior model (Figure 7.9) was computed as the best transformation fitting the reference landmarks on to the target landmarks. The obtained mean of the posterior model was the patient-specific approximated 3D model of the scapula from 2D X-ray images using landmark-constrained SSM fitting. In the sections to follow, the computed mean shape of the posterior model is referred to as the approximated 3D model.

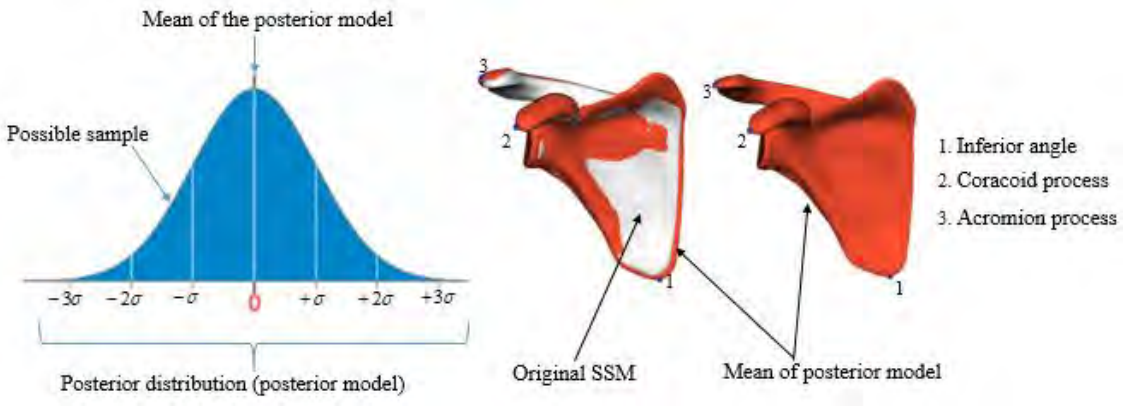

Figure 7.9: The approximated 3D model (red) computed from the aligned SSM (grey). The approximated 3D model's landmarks fit on to the corresponding target landmarks (blue points on model). The mean of the posterior model gives the best an unbiased fit with a standard error of the mean equals to zero (blue graph).

7.4 Validation of the approximated 3D model

7.4.1 CT data used for validation of the approximated 3D model

CT scan of scapula bone of an adult cadaveric shoulder was used to obtain a CT ground truth image against which the approximated 3D model was validated. Image segmentation, a technique of dividing a digital image into multiple parts for easy analysis and information extraction, was carried out on the shoulder CT scan to extract the scapula bone. Amira software (*FEI* Visualization Sciences Group, France) was used for this component of the research. Amira is a 3D software for visualizing and segmenting data acquired using imaging modalities like CT and MRI.

7.4.2 Experiment 1: Comparison between the approximated 3D model and the CT ground truth image

The first experiment was to compute the surface-to-surface average distance between the approximated 3D model and the CT ground truth image. The average distance (section 3.7.5) was computed using the **avgDistance** method implemented in Scalismo which returns the average distance between two aligned meshes.

An average distance of 4.28 mm was obtained between the aligned CT ground truth image and the approximated 3D model (Figure 7.10).

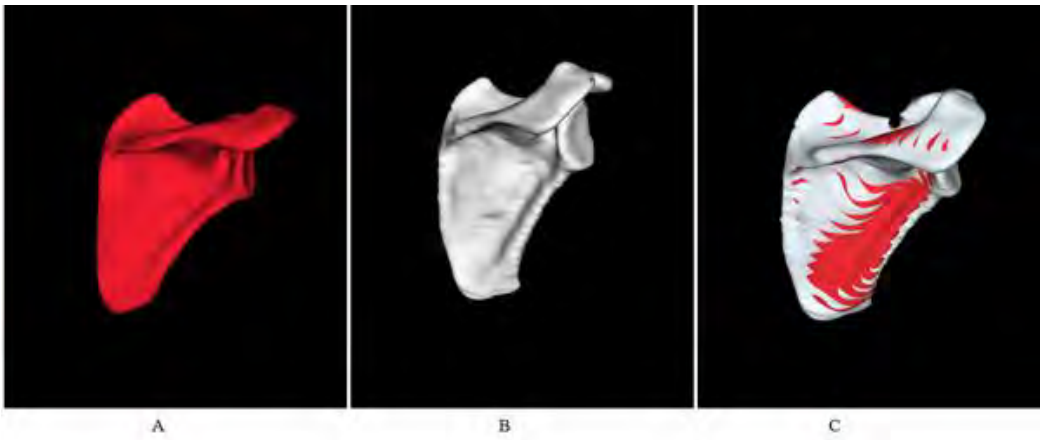

Figure 7.10: (A) Approximated 3D model, (B) CT ground truth image, (C) Approximated 3D model and CT ground truth image aligned.

The approximated 3D model (Figure 7.10.A) was constrained to fit to the target landmarks using a lower number (3) of landmarks (inferior angle, acromion and coracoid process). Hence, the computed model is not a full surface-to-surface fit on to the CT ground truth image (Figure 7.10.C) as it lacks information about the deformations at various points.

7.4.3 Experiment 2: Euclidean distances between the selected landmarks on the approximated 3D model and the corresponding landmarks on CT ground truth image

The second experiment was to determine the Euclidean distances between the selected landmarks on the approximated 3D model and the corresponding landmarks on the CT ground truth image (Figure 7.11). Furthermore, the Euclidean distances between the selected landmarks on the original SSM and the corresponding landmarks on the CT ground truth image were determined.

The Euclidean distances (section 3.7.3) were computed using equation [3.33].

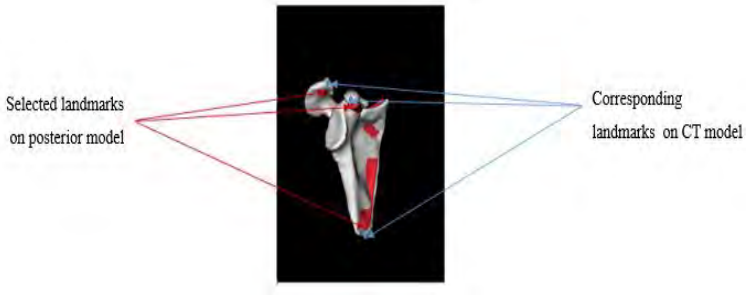

Figure 7.11: The approximated 3D model (red) aligned with the CT ground truth image (grey) to compare the Euclidean distances between selected corresponding landmarks.

The target landmarks (reconstructed 3D coordinates from 2D X-ray images) were obtained from a 2D X-ray image of a scapula obtained from the cadaveric shoulder radiography. The same cadaveric shoulder was CT scanned to obtain the ground truth image. Hence, the target landmarks are expected to be close to the corresponding landmarks on the CT image.

The results of the Euclidean distances between the selected landmarks on the approximated 3D model and the corresponding landmarks on the CT ground truth image are shown in Table 7.2.

Table 7.2: The Euclidean distances between the selected landmarks on the approximated 3D model and the corresponding landmarks on the CT ground truth image.

Landmark	Approximated model's coordinates (mm)			CT ground truth coordinates (mm)			Euclidean distances (mm)
	X	Y	Z	X	Y	Z	
Inferior angle	180.46	274.87	10.81	182.01	275.04	10.89	1.56
Coracoid	159.56	110.91	66.19	159.42	111.82	67.02	1.23
Acromion	140.13	85.02	26.90	139.54	85.65	25.99	1.25

An average Euclidean distance of 1.35 mm was obtained. The selected landmarks on the approximated 3D model moved closer to the corresponding landmarks on the CT ground truth image.

Results of the Euclidean distances between the selected landmarks on the original SSM and the corresponding landmarks on the CT ground truth image are shown in Table 7.3.

Table 7.3: The Euclidean distances between the selected landmarks on the original SSM and the corresponding landmarks on the CT ground truth image.

Landmark	Original SSM landmarks' coordinates (mm)			CT ground truth coordinates (mm)			Euclidean distances (mm)
	X	Y	Z	X	Y	Z	
Inferior angle	178.03	270.24	13.54	182.01	275.04	10.89	6.77
Coracoid	157.23	111.27	63.00	159.42	111.82	67.02	4.61
Acromion	139.46	87.98	32.16	139.54	85.65	25.99	6.59

An average Euclidean distance of 5.99 mm was obtained compared with an average Euclidean distance of 1.35 mm between the landmarks on the approximated 3D model and the CT ground truth image. Thus posterior model reduces the search space for the patient-specific 3D model by approximating the possible shape of the 3D model given some parameters (landmarks in this case).

7.4.4 Experiment 3: Euclidean distances between the target landmarks and the corresponding landmarks on the approximated 3D model

The third experiment was to determine the Euclidean distances between the target landmarks and the corresponding landmarks on the approximated 3D model. Furthermore, the Euclidean distances between the target landmarks and the selected landmarks on the original SSM were determined.

The Euclidean distances were computed after a rigid alignment of the target coordinates with the approximated 3D model (Figure 7.12). This experiment was necessary to assess if the selected landmarks on the posterior model moved closer to the target landmarks during the fitting process.

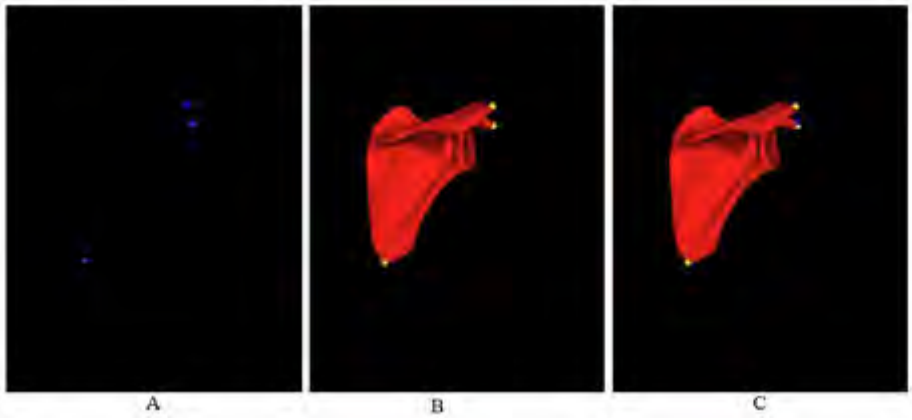

Figure 7.12: (A) Target landmarks (blue points), (B) Corresponding landmarks on approximated 3D model (yellow) and (C) Approximated 3D model landmark fit to the corresponding target landmarks.

Results of the Euclidean distances between the target landmarks and the corresponding landmarks on the approximated 3D model are shown in Table 7.4.

Table 7.4: Euclidean distances between the target landmarks and corresponding landmarks on the approximated 3D model.

Landmark	Target coordinates (mm)			Approximated model's coordinates (mm)			Euclidean distances (mm)
	X	Y	Z	X	Y	Z	
Inferior angle	180.00	274.92	10.90	180.46	274.87	10.81	0.47
Coracoid	159.93	110.95	66.17	159.56	110.91	66.19	0.37
Acromion	140.19	85.259	26.31	140.13	85.02	26.90	0.63

Similarly to Table 7.4 results of the Euclidean distances between the target landmarks and the corresponding landmarks on the original SSM are shown in Table 7.5.

Table 7.5: Euclidean distances between the target landmarks and corresponding landmarks on the original SSM.

Landmark	Target coordinates (mm)			Original SSM landmarks' coordinates (mm)			Euclidean distance (mm)
	X	Y	Z	X	Y	Z	
Inferior angle	180.00	274.92	10.90	179.56	268.91	12.53	6.24
Coracoid	159.93	110.95	66.17	161.56	113.99	61.01	6.21
Acromion	140.19	85.259	26.31	137.93	88.99	24.06	4.91

The selected landmarks on the approximated 3D model moved closer to the target landmarks with an average Euclidean distance of 0.49 mm (Table 7.4), compared with an original average distance of 5.78 mm (Table 7.5) between the original SSM and the target coordinates.

The error between the target coordinates and the corresponding landmarks on the approximated 3D model is attributed to the manual landmarking of the corresponding points on the posterior model and the low number of landmarks (three) used to establish the point-to-point correspondences between the target and reference landmarks. In an error-free system with more landmarks used, the reference landmarks are expected to be closer to or to perfectly fit the target landmarks (Lüthi et al., 2011).

7.4.5 Experiment 4: Inter-landmark distances between pairs of target landmarks and the corresponding pair of landmarks on the approximated 3D model.

The fourth experiment was to determine the inter-landmark distances between pairs of target landmarks and the corresponding pairs of landmarks on the approximated 3D model. This was necessary to assess if the transformation, during resolving the coordinate system differences, was rigid and there was no change in the shape of the model. The inter-landmark distances (section 3.7.4) were computed using equation [3.34].

In Table 7.6, **ILD^1** are the inter-landmark distances between inferior angle and coracoid process; and between coracoid process and acromion of the target landmarks. Similarly, **ILD^2** are the inter-landmark distances between inferior angle and coracoid process; and between coracoid process and acromion of the corresponding landmarks on the approximated 3D model.

Table 7.6: Inter-landmark distance between the target landmarks and corresponding landmarks on the approximated 3D model.

No.	Target coordinates (mm)			Approximated model's coordinates (mm)			ILD^1 (mm)	ILD^2 (mm)	E (mm)
	X	Y	Z	X	Y	Z			
1	180.00	274.92	10.90	180.46	274.87	10.81	174.19	174.31	0.12
2	159.93	110.95	66.17	159.56	110.91	66.19	51.36	50.90	0.45
3	140.19	85.25	26.31	140.13	85.02	26.90			

(1) Inferior angle, (**2**) Coracoid, (**3**) Acromion

Inter-landmark distances obtained between the pair of target landmarks and the corresponding pair of landmarks on the approximated 3D model were very close to each other with an average difference, **E** of 0.29 mm.

7.4.6 Experiment 5: Increasing number of identifiable landmarks on the scapula

Tests to assess how increasing the number of identifiable landmarks on the scapula affects the accuracy of the approximation were conducted. This was done by comparing surface-to-surface distances (Hausdorff, average and Procrustes distances) (section 3.7) between the approximated 3D model and the CT ground truth image using three and sixteen landmarks.

Two tests were conducted: The first one used an instance from the SSM. The second test used data from outside the SSM training set.

In each case radio-opaque steel bearings, 2 mm in diameter, were embedded on sixteen biomechanically significant anatomical landmarks (Borotikar et al., 2015) of an instance that was 3D printed. A clinician was consulted to select the desired landmarks on each of the instances; one from the SSM (a random instance from SSM) and the other external to the SSM (obtained from a random CT scan of a scapula) (Figure 7.13).

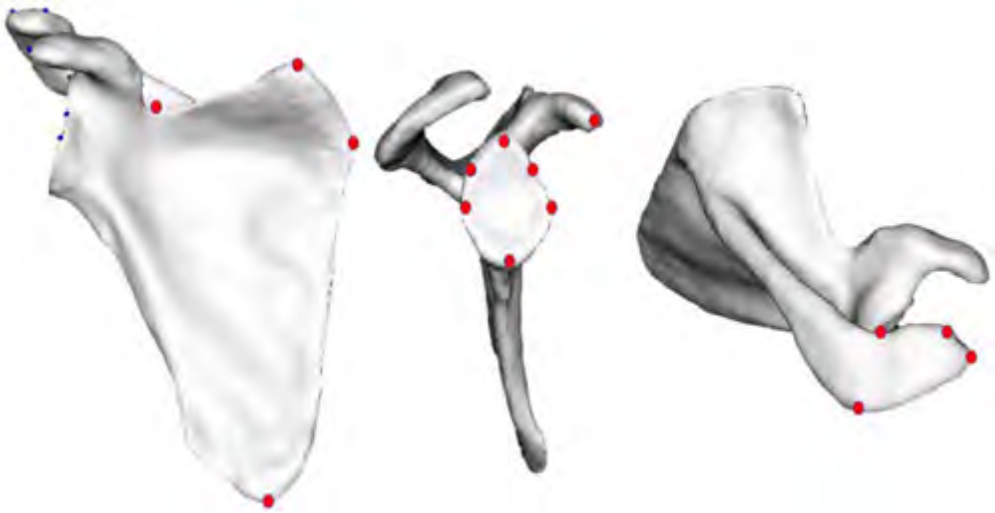

Figure 7.13: SSM instance showing the positions (red circles) where the steel bearings were embedded.

Both of the 3D printed test instances were scanned from two perspectives using Lodox Statscan system and the calibration frame and volume described in section 4.2 to obtain bi-planar 2D X-ray images (Figure 7.14).

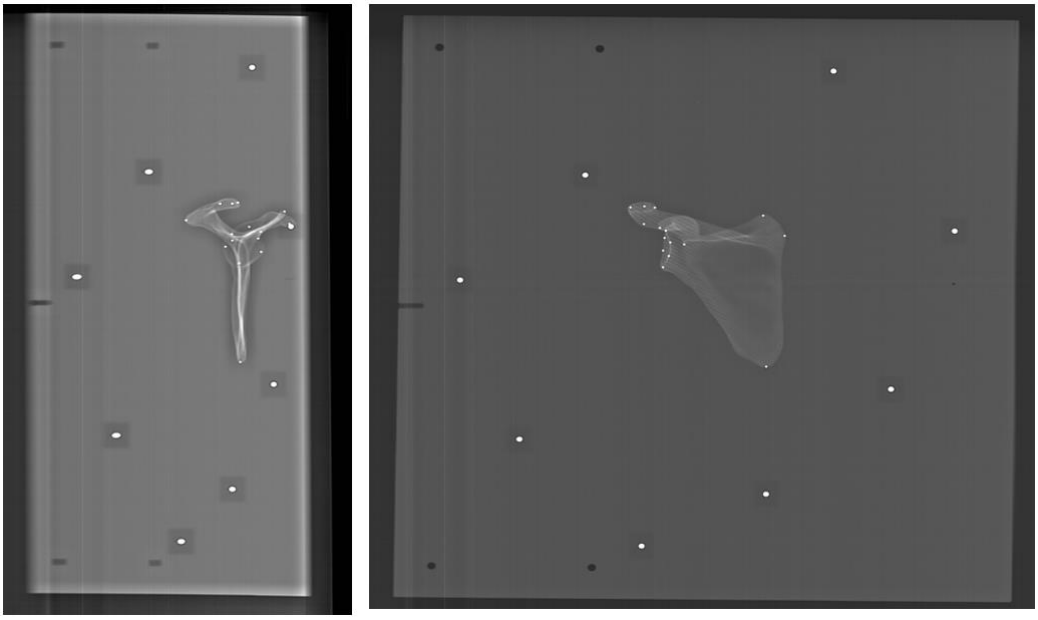

Figure 7.14: Bi-planar 2D X-ray images of the 3D printed scapula with small ball bearings located at sixteen landmarks for 3D coordinates reconstruction.

The obtained bi-planar 2D X-ray images were used to reconstruct the 3D coordinates of the sixteen landmarks clearly defined by the steel bearings using the developed 3D localization tool (Figure 7.15). Epipolar geometry guided the corresponding point search in the second view.

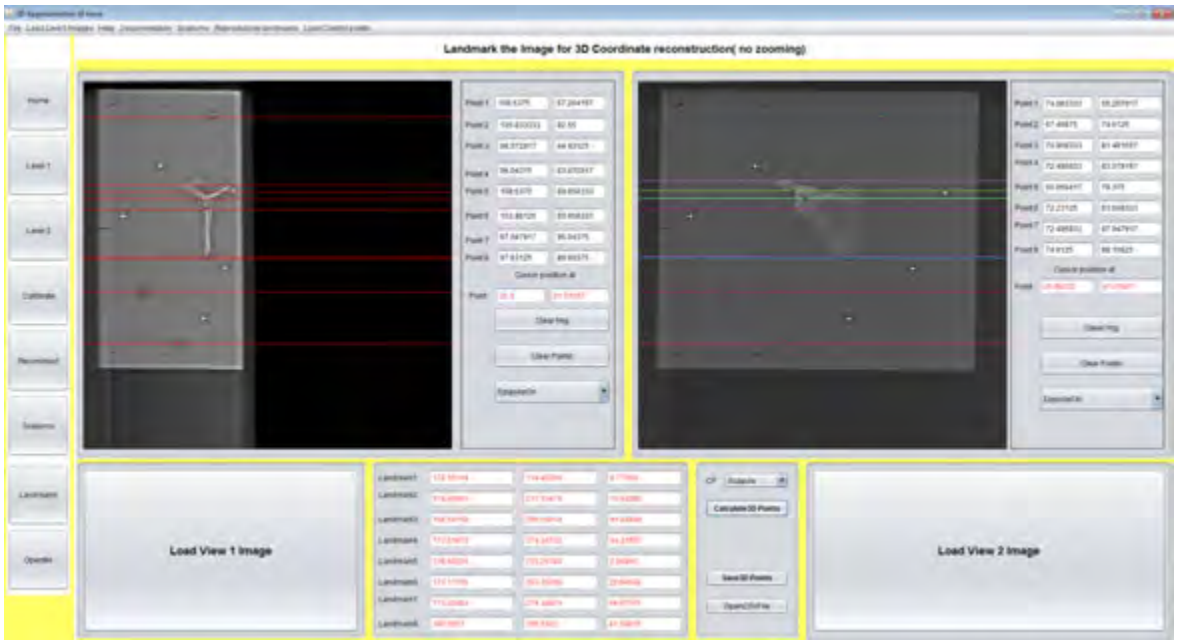

Figure 7.15: GUI for 3D point localization with the help of epipolar geometry in the corresponding view to aid the search for the matching point.

Based on the sixteen reconstructed landmarks (Figure 7.15), a mean of the posterior model was computed from the original SSM using the fitting algorithm (Figure 7.16) described in section 7.3 for each of the test cases. The approximated 3D models were compared with the CT ground truth image.

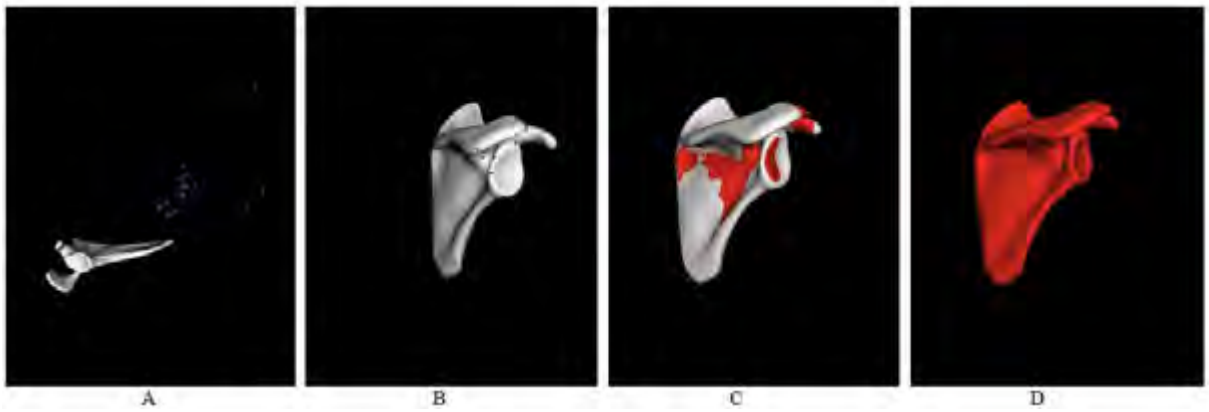

Figure 7.16: (A) Target landmarks (blue) and reference SSM, (B) Translated SSM aligned with target landmarks, (C) Mean of posterior model computed from translated SSM and (D) Approximated 3D model constrained to the target landmarks.

Similarly, another mean shape from the posterior model was computed from the original SSM using only three landmarks for each test case. Sixteen and three landmarks were used as these were the maximum and minimum of number of biomechanically significant landmarks on the scapula that could clearly be selected by a clinician.

The results of the modified Hausdorff, average and Procrustes distances between the CT ground truth image and approximated 3D models using three and sixteen landmarks selected from an object from the SSM training dataset are shown in Tables 7.7.

Table 7.7: Modified Hausdorff, average and Procrustes distances obtained using three and sixteen landmarks to fit a SSM to data from within the training dataset.

Number of landmarks	**Similarity measure metric (mm)**		
	Modified Hausdorff	Average distance	Procrustes
3	3.49	3.20	0.09
16	2.94	2.46	0.04

The distances obtained showed that increasing the number of landmarks results in lower surface-to-surface distances between the approximated 3D model and the CT ground truth

image, hence increasing the possibility of producing a posterior model that makes better predictions of a patient-specific 3D model.

The surface-to-surface distances between the CT ground truth image and approximated 3D models using three and sixteen landmarks selected from an object outside the SSM training dataset are shown in Table 7.8.

Table 7.8: Modified Hausdorff, average and Procrustes distances obtained using sixteen and three landmarks to fit a SSM to data from outside the training dataset.

Number of landmarks	Similarity measure metric (mm)		
	Modified hausdorff	Average distance	Procrustes
3	4.34	4.28	0.24
16	3.42	3.20	0.16

Similarly to Table 7.6, increasing the number of landmarks results into lower surface-to-surface distances.

7.5 Discussion of 3D reconstruction validation results

7.5.1 Comparison between the approximated 3D model and the CT ground truth image

The surface-to-surface distances obtained between the approximated 3D model and the CT ground truth image were greater than 0 mm, a case for perfectly similar objects. This is attributed to the fact that the SSM was constrained using only three landmarks (Experiment 1) and hence it lacked information on the deformations at various points. With more landmarks however, lower errors between the CT ground truth image and the approximated model were obtained (Table 7.8).

Furthermore, the differences between the approximated 3D model and the ground truth CT image can be attributed to a lack of information in the approximated model about point-specific intensities, which are captured using CT. This is a limitation of the presented method, due to only landmarks being used to produce a patient-specific 3D model constrained at the selected landmarks. However, the mean of the posterior model (approximated 3D model) is close to the ground truth image and the search space for exact patient-specific 3D model by other fitting algorithms is reduced by the approach. Utilization of intensity-based fitting algorithms facilitates the fitting of the whole image to an intensity

model which may overcome the limitation of using a low number of landmarks (Rohr et al., 2006).

7.5.2 Euclidean distance between the selected landmarks on the approximated 3D model and the corresponding landmarks on CT ground truth image

The average Euclidean distance between the landmarks on the approximated 3D model and the corresponding landmarks on CT ground truth image shows that the approximated 3D model is closer to the CT ground truth image than the original SSM (Table 7.3).

7.5.3 Euclidean distance between the target landmarks and corresponding landmarks on the approximated 3D model

Similarly, the average Euclidean distance between the target landmarks and the corresponding landmarks on the approximated 3D model shows that the selected landmarks on the approximated 3D model moved closer to the target landmarks (Table 7.4). The target landmarks were reconstructed from 2D X-ray images of the same scapula from which the CT ground truth image was obtained. Thus 3D patient-specific models can be obtained from 2D X-ray images.

7.5.4 Inter-landmark distances between the target landmarks and corresponding landmarks on the approximated 3D model

The inter-landmark distances between target landmarks and corresponding landmarks on the approximated 3D model show that the shape of the model was preserved during the transformation of the SSM into the target coordinate system. Inter-landmark distance measurements are very useful in diagnosis and surgery planning and have been used for different clinical applications (Sanders et al., 2009; Douglas et al., 2012). Hence, the developed 3D localization tool can be used for similar applications if the desired landmarks on the 2D image can be selected using the tool. Similar results would be expected for inter-landmark distances obtained from a 3D image obtained using CT or MRI.

7.5.5 Increasing the number of identifiable landmarks on the scapula

The surface-to-surface distances obtained in section 7.4.6 show that increasing the number of landmarks for SSM fitting produces a posterior model that makes better predictions of patient-specific 3D models. This is shown by lower surface-to-surface distances obtained with sixteen landmarks compared to three landmarks. Methods like delineation of contours using image processing to obtain more landmarks could potentially result in a model that is better constrained and closer to the ground truth image.

8 CONCLUSIONS AND RECOMMENDATIONS

The overall aim of this research was to approximate a patient-specific 3D model of a scapula bone from 2D X-ray images using landmark-constrained statistical shape model fitting. This included developing a GUI for 3D coordinate localization, then developing an algorithm to fit a SSM on the 3D reconstructed coordinates from 2D X-ray images. The output is a 3D model approximation pipeline.

8.1 Summary of findings

8.1.1 The 3D model approximation pipeline is user friendly

- The developed GUI is easy to use.
- The epipolar geometry makes it easy to select the corresponding point in second view.
- Automatic computation of control image points reduces the time required to compute the transformation parameters.
- The landmark-constrained fitting algorithm is easy to use.

8.1.2 Epipolar geometry improves 3D coordinates reconstruction accuracy

Three-dimensional coordinate reconstruction was based on bi-planar 2D image points. Hence, errors in the 2D landmarking results in errors in the reconstructed 3D coordinates. Without the epipolar geometry, it was difficult to select the corresponding image point in the second view. However, epipolar geometry implementation alleviated this problem increasing the accuracy of 2D image point landmarking.

8.1.3 Increasing the number of identifiable landmarks improves the 3D model approximations

Although three landmarks were adequate to obtain an initial approximation of a patient-specific 3D model using landmark-constrained SSM fitting, it was observed that increasing the number of landmarks resulted into a posterior distribution whose mean shape is closer to the CT ground truth image.

8.1.4 The 3D model approximation pipeline can potentially work for other bones

The presented 3D model approximation pipeline was developed for the scapula bone after a literature review of what has been done in this field and considering the clinical significance of the scapula bone. The successful results obtained for the scapula bone, considered a complex bone of the body, suggest that the developed pipeline would be suitable for other bones.

8.1.5 The approximated 3D model of the scapula bone has a range of applications

- The approximated 3D model reduces the search space for other fitting algorithms. These include intensity based fitting algorithms (Rohr et al., 2006) and point distribution models (Hill and Taylor, 1994) that can be applied on the approximated 3D model to produce patient-specific exact 3D models.
- Patient-specific exact 3D models can be used in a range of medical applications like pre-surgery planning and prosthesis design.

8.2 Overall limitations of the developed tool and recommendations for future work

The 3D model application pipeline constitutes two separate modules (the 3D localization tool and the fitting platform implemented in Scalismo) which makes it more demanding to use. Having the two modules combined into a single tool would simplify the use of the pipeline, making it more accessible in a clinical setting.

The approximated model was computed using only three landmarks which were identifiable using the developed tool. It is however recommended that other fitting algorithms like contour fitting be explored, to increase the number of available landmarks.

The SSM used was built from normal data, without biological deformation. Deformations may not be captured in the approximated model. Lastly the reconstruction technique was tested on one cadaveric specimen. It is therefore recommended that other extensive tests with several cadavers be carried out. This will allow an evaluation of the general applicability of the technique.

8.3 Overall conclusion and contribution of the project

A 3D localization tool with epipolar geometry has been developed and validated. This is an improvement on the 3D localization method developed by Chimhundu et al. (2014) to a more user friendly GUI developed in a language interoperable with Scalismo, an open source shape modelling platform. The tool can be used for other research where 3D coordinates from bi-planar 2D X-ray images are required.

A landmark-constrained SSM fitting algorithm has been developed. Selecting three landmarks from bi-planar 2D X-ray images of a scapula using the developed 3D reconstruction pipeline enables easy, fast and accurate approximation of a patient-specific 3D model of a scapula. The approximated 3D model helps to reduce the search space for more accurate 3D patient-specific model which may be obtained other fitting algorithms. The methodology presented here is transferable to other bones.

REFERENCES

Abdel-Aziz, Y. I., & Karara, H. M. (2015). Direct Linear Transformation from Comparator Coordinates into Object Space Coordinates in Close-Range Photogrammetry. *Photogrammetric Engineering & Remote Sensing*, *81*(2), 103–107. http://doi.org/10.14358/PERS.81.2.103

Adams, L. P. (1981). X-ray stereo photogrammetry locating the precise, three-dimensional position of image points. *Medical & Biological Engineering & Computing*, *19*(5), 569–578. http://doi.org/10.1007/BF02442771

Al-Aifari, R., Daubechies, I., & Lipman, Y. (2013). Continuous Procrustes distance between two surfaces. *Communications on Pure and Applied Mathematics*, *66*(6), 934–964. http://doi.org/10.1002/cpa.21444

Aldroubi, A., & Sekmen, A. (2014). Reduced row echelon form and non-linear approximation for subspace segmentation and high-dimensional data clustering. *Applied and Computational Harmonic Analysis*, *37*(2), 271–287. http://doi.org/10.1016/j.acha.2013.12.001

Allen, G. I., Grosenick, L., & Taylor, J. (2014). A Generalized Least-Square Matrix Decomposition. *Journal of the American Statistical Association*, *109*(505), 145–159. http://doi.org/10.1080/01621459.2013.852978

Andrew, G., Arora, R., Bilmes, J., & Livescu, K. (2013). Deep Canonical Correlation Analysis. *Proceedings of The 30th International Conference on Machine Learning*, *28*, 1247–1255.

Baka, N., Kaptein, B. L., de Bruijne, M., van Walsum, T., Giphart, J. E., Niessen, W. J., & Lelieveldt, B. P. F. (2011). 2D-3D shape reconstruction of the distal femur from stereo X-ray imaging using statistical shape models. *Medical Image Analysis*, *15*(6), 840–850. http://doi.org/10.1016/j.media.2011.04.001

Basta, T. (2014). Is the Fundamental Matrix Really Independent of the Scene Structure ? *International Journal of Signal Processing, Image Processing and Pattern Recognition*, *7*(5), 149–168. http://doi.org/http://dx.doi.org/10.14257/ijsip.2014.7.5.13

Bilionis, I., & Zabaras, N. (2012). Multi-output local Gaussian process regression: Applications to uncertainty quantification. *Journal of Computational Physics*, *231*(17), 5718–5746. http://doi.org/10.1016/j.jcp.2012.04.047

Borgonovo, E. (2007). A new uncertainty importance measure. *Reliability Engineering and*

System Safety, *92*(6), 771–784. http://doi.org/10.1016/j.ress.2006.04.015

Borotikar, B., Ghorbel, E., Lempereur, M., Mutsvangwa, T., & Burdin, V. (2015). Evaluation of an anatomically augmented Statistical Shape Model of the scapula: Clinical validation and reliability of landmark selection. Submited to *Computer Methods in Biomechanics and Biomedical Engineering: Imaging & Visualization* Journal.

Brenner, D. J., & Elliston, C. D. (2004). Estimated radiation risks potentially associated with full-body CT screening. *Radiology*, *232*(3), 735–738. http://doi.org/10.1148/radiol.2323031095

Burgstaller, B., & Pillichshammer, F. (2009). The Average Distance Between Two Points. *Bulletin of the Australian Mathematical Society*, *80*(03), 353–359. http://doi.org/10.1017/S0004972709000707

Burns, J. B., Hanson, A. R., & Riseman, E. M. (1986). Extracting Straight Lines. *IEEE Transactions on Pattern Analysis and Machine Intelligence*, *PAMI-8*(4), 425–455. http://doi.org/10.1109/TPAMI.1986.4767808

Challis, J. H. (1995). A procedure for determining rigid body transformation parameters. *Journal of Biomechanics*, *28*(6), 733–737. http://doi.org/10.1016/0021-9290(94)00116-L

Chapman, H. N., Fromme, P., Barty, A., White, T. a, Kirian, R. a, Aquila, A., … Spence, J. C. H. (2011). Femtosecond X-ray protein nanocrystallography. *Nature*, *470*(7332), 73–77. http://doi.org/10.1038/nature09750

Chapter, T. (1999). Java™ 2D graphics. *Computers & Mathematics with Applications*, *38*(11-12), 282. http://doi.org/10.1016/S0898-1221(99)91191-4

Chen, H., Rogalski, M. M., & Anker, J. N. (2012). Advances in functional X-ray imaging techniques and contrast agents. *Physical Chemistry Chemical Physics : PCCP*, *14*(39), 13469–86. http://doi.org/10.1039/c2cp41858d

Chen, L. (1994). An investigation on the accuracy of three-dimensional space reconstruction using the direct linear transformation technique. *Journal of Biomechanics*, *27*(4), 493–500. http://doi.org/10.1016/0021-9290(94)90024-8

Chimhundu, C., Sivarasu, S., Steiner, S., Smit, J., & Douglas, T. S. (2016). Femoral neck anteversion measurement using linear slot scanning radiography. *Medical Engineering and Physics*, *38*(2), 187–191. http://doi.org/10.1016/j.medengphy.2015.11.017

Chimhundu, C., Smit, J., Sivarasu, S., & Douglas, T. S. (2014). Interlandmark Measurements From Lodox Statscan Images1. *Journal of Medical Devices*, *8*(3), 30908. Retrieved from http://dx.doi.org/10.1115/1.4027102

Coleman, T., & Pothen, A. (1986). The Null Space Problem I. Complexity. *SIAM Journal on Algebraic Discrete Methods*, *7*(4), 527–537. http://doi.org/10.1137/0607059

Cook, C. (2000). A Review of Intraclass Correlation. *Annual Meeting of the Southwest Educational Research Association*.

Cootes, T. F., Taylor, C. J., Cooper, D. H., & Graham, J. (1992). Training models of shape from sets of examples. *BMVC*, 9–18. http://doi.org/10.1017/CBO9781107415324.004

Cootes, T. F., Taylor, C. J., Cooper, D. H., & Graham, J. (1995). Active Shape Models-Their Training and Application. *Computer Vision and Image Understanding*, *61*(1), 38–59. http://doi.org/10.1006/cviu.1995.1004

Crum, W. R. (2004). Non-rigid image registration: theory and practice. *British Journal of Radiology*. http://doi.org/10.1259/bjr/25329214

Crum, W. R., Hartkens, T., & Hill, D. L. G. (2004). Non-rigid image registration: theory and practice. *The British Journal of Radiology*, *77*, S140–S153. http://doi.org/10.1259/bjr/25329214

Danielsson, P. E. (1980). Euclidean distance mapping. *Computer Graphics and Image Processing*, *14*(3), 227–248. http://doi.org/10.1016/0146-664X(80)90054-4

Douglas, T. S. (2004). Image processing for craniofacial landmark identification and measurement: A review of photogrammetry and cephalometry. *Computerized Medical Imaging and Graphics*. http://doi.org/10.1016/j.compmedimag.2004.06.002

Douglas, T. S., Vaughan, C. L., & Wynne, S. M. (2004). Three-dimensional point localisation in low-dose X-ray images using stereo-photogrammetry. *Medical and Biological Engineering and Computing*, *42*(1), 37–43. http://doi.org/10.1007/BF02351009

Dubuisson, M., & Jain, A. K. (1994). A Modi ed Hausdor Distance for Object Matching. *International Conference on Pattern Recognition*, 566–568. http://doi.org/10.1109/ICPR.1994.576361

Dubuisson, M.-P., & Jain, a. K. (1994). A modified Hausdorff distance for object matching. *Proceedings of 12th International Conference on Pattern Recognition*, *1*(1), 566–568. http://doi.org/10.1109/ICPR.1994.576361

Dworzak, J., Lamecker, H., Von Berg, J., Klinder, T., Lorenz, C., Kainmüller, D., … Zachow, S. (2010). 3D reconstruction of the human rib cage from 2D projection images using a statistical shape model. *International Journal of Computer Assisted Radiology and Surgery*, *5*(2), 111–124. http://doi.org/10.1007/s11548-009-0390-2

Fitzmaurice, G. (2002). Measurement error and reliability. In *Nutrition* (Vol. 18, pp. 112–

114). http://doi.org/10.1016/S0899-9007(01)00624-4

Gamage, P., Xie, S. Q., Delmas, P., & Xu, P. (2009). 3D reconstruction of patient specific bone models from 2D radiographs for image guided orthopedic surgery. *DICTA 2009 - Digital Image Computing: Techniques and Applications*, 212–216. http://doi.org/10.1109/DICTA.2009.42

Glóer, C. C., Blake, G., Lu, Y., Blunt1, B. A., Jergas1, M., & Genant1, H. K. (1995). Accurate assessment of precision errors: How to measure the reproducibility of bone densitometry techniques. *Osteoporosis International*, *5*(4), 262–270. http://doi.org/10.1007/BF01774016

Gold, G. E., Chen, C. A., Koo, S., Hargreaves, B. A., & Bangerter, N. K. (2009). Recent advances in MRI of articular cartilage. *American Journal of Roentgenology*. http://doi.org/10.2214/AJR.09.3042

Golub, G. H., & Reinsch, C. (1970). Singular value decomposition and least squares solutions. *Numerische Mathematik*, *14*(5), 403–420. http://doi.org/10.1007/BF02163027

Goodman, S. (2008). A Dirty Dozen: Twelve P-Value Misconceptions. *Seminars in Hematology*, *45*(3), 135–140. http://doi.org/10.1053/j.seminhematol.2008.04.003

Góra, P., & Boyarsky, A. (1988). Why computers like lebesgue measure. *Computers and Mathematics with Applications*, *16*(4), 321–329. http://doi.org/10.1016/0898-1221(88)90148-4

Hall, E. J., & Brenner, D. J. (2008). Cancer risks from diagnostic radiology. *The British Journal of Radiology*, *81*(965), 362–378. http://doi.org/10.1259/bjr/01948454

Hartley, R. I. (1997). In defense of the eight-point algorithm. *IEEE Transactions on Pattern Analysis and Machine Intelligence*, *19*(6), 580–593. http://doi.org/10.1109/34.601246

Hartley, R., & Zissermann, A. (2009). Epipolar Geometry and the Fundamental Matrix. *Multiple View Geometry Chapter 9*, 1–23.

Hassner, T., & Rehovot, S. (2006). Example Based 3D Reconstruction from Single 2D Images. *Science*, *00*(c), 0–7.

Heimann, T., & Meinzer, H.-P. (2009). Statistical shape models for 3D medical image segmentation: a review. *Medical Image Analysis*, *13*(4), 543–63. http://doi.org/10.1016/j.media.2009.05.004

Heinonen, T., Visala, K., Blomqvist, M., Eskola, H., & Frey, H. (1998). 3D visualization library for multimodal medical images. *Computerized Medical Imaging and Graphics*, *22*(4), 267–273. http://doi.org/10.1016/S0895-6111(98)00031-7

Helmke, U., Hüper, K., Lee, P. Y., & Moore, J. (2007). Essential matrix estimation using

Gauss-Newton iterations on a manifold. *International Journal of Computer Vision*, *74*(2), 117–136. http://doi.org/10.1007/s11263-006-0005-0

Hemrajani, A. (1996). The Java Abstract Window Toolkit. *Dr. Dobb's Journal of Software Tools*, *21*(9), 40, 42, 44.

Higham, N. J. (2011). Gaussian elimination. *Wiley Interdisciplinary Reviews: Computational Statistics*, *3*(3), 230–238. http://doi.org/10.1002/wics.164

Hill, a, & Taylor, C. J. (1994). Automatic Landmark Generation for Point Distribution Models. *British Machine Vision Conference*, 429–438. http://doi.org/10.5244/C.8.42

Horn, B. K. P. (1990). Recovering Baseline and Orientation from Essential Matrix. *[Online: 04.06.2014]*, (January), http://ocw.mit.edu/courses/.

Hulstyn, M. J., & Fadale, P. D. (1997). Shoulder injuries in the athlete. *Clinics in Sports Medicine*. http://doi.org/10.1016/S0278-5919(05)70047-8

Hurvitz, A., & Joskowicz, L. (2008). Registration of a CT-like atlas to fluoroscopic X-ray images using intensity correspondences. *International Journal of Computer Assisted Radiology and Surgery*, *3*(6), 493–504. http://doi.org/10.1007/s11548-008-0264-z

Irving, B. J., Maree, G. J., Hering, E. R., & Douglas, T. S. (2008). Radiation dose from a linear slit scanning X-ray machine with full-body imaging capabilities. *Radiation Protection Dosimetry*, *130*(4), 482–489. http://doi.org/10.1093/rpd/ncn073

Iwashita, Y., Kurazume, R., Tsuji, T., Hasegawa, T., & Hara, K. (2004). Fast implementation of level set method and its real-time applications. In *Systems, Man and Cybernetics* (Vol. 7, pp. 6302–6307). http://doi.org/10.1109/ICSMC.2004.1401389

Kalender, W. A. (2006). X-ray computed tomography. *Physics in Medicine and Biology*, *51*(13), R29–R43. http://doi.org/10.1088/0031-9155/51/13/R03

Kelley, B. P., Brown, S. P., Warren, G. L., & Muchmore, S. W. (2015). POSIT: Flexible Shape-Guided Docking for Pose Prediction. *Journal of Chemical Information and Modeling*, *55*(8), 1771–1780. http://doi.org/10.1021/acs.jcim.5b00142

Kibler, W. B. (2015). The role of the scapula in athletic shoulder function. *The American Journal of Sports Medicine*, *26*(2), 325–37. http://doi.org/10.1177/0363546598026002801

Kotsas, P. D., & Dodd, T. (2011). A Review of Methods for 2D / 3D Registration, 606–609.

Kurazume, R., Nakamura, K., Okada, T., Sato, Y., Sugano, N., Koyama, T., … Hasegawa, T. (2009). 3D reconstruction of a femoral shape using a parametric model and two 2D fluoroscopic images. *Computer Vision and Image Understanding*, *113*(2), 202–211. http://doi.org/10.1016/j.cviu.2008.08.012

Laporte, S., Skalli, W., de Guise, J. A., Lavaste, F., & Mitton, D. (2003). A biplanar reconstruction method based on 2D and 3D contours: application to the distal femur. *Computer Methods in Biomechanics and Biomedical Engineering*, *6*(1), 1–6. http://doi.org/10.1080/1025584031000065956

Ledoit, O., & Wolf, M. (2004). A well-conditioned estimator for large-dimensional covariance matrices. *Journal of Multivariate Analysis*, *88*(2), 365–411. http://doi.org/10.1016/S0047-259X(03)00096-4

Liberti, L., Lavor, C., Maculan, N., & Mucherino, A. (2014). Euclidean Distance Geometry and Applications. *SIAM Review*, *56*(1), 3–69. http://doi.org/10.1137/120875909

Lin, J.-J., Hanten, W. P., Olson, S. L., Roddey, T. S., Soto-Quijano, D. a, Lim, H. K., & Sherwood, A. M. (2005). Functional activities characteristics of shoulder complex movements: Exploration with a 3-D electromagnetic measurement system. *Journal of Rehabilitation Research and Development*, *42*(2), 199–210. http://doi.org/10.1682/JRRD.2004.04.0045

López Puga, J., Krzywinski, M., & Altman, N. (2015). Bayes' theorem. *Nature Publishing Group*, *12*(4), 277–278. http://doi.org/10.1038/nmeth.3335

Lüthi, M., Jud, C., & Vetter, T. (2011). Using landmarks as a deformation prior for hybrid image registration. In *Lecture Notes in Computer Science (including subseries Lecture Notes in Artificial Intelligence and Lecture Notes in Bioinformatics)* (Vol. 6835 LNCS, pp. 196–205). http://doi.org/10.1007/978-3-642-23123-0_20

Mackey, D. S., Mackey, N., Mehl, C., & Mehrmann, V. (2013). Skew-symmetric matrix polynomials and their Smith forms. *Linear Algebra and Its Applications*, *438*(12), 4625–4653. http://doi.org/10.1016/j.laa.2013.02.010

Mantokoudis, G., Hegner, S., Dubach, P., Bonel, H. M., Senn, P., Caversaccio, M. D., & Exadaktylos, A. K. (2013). How reliable and safe is full-body low-dose radiography (LODOX Statscan) in detecting foreign bodies ingested by adults? *Emergency Medicine Journal : EMJ*, *30*(7), 559–564. http://doi.org/10.1136/emermed-2011-200911

Markelj, P., Tomaževič, D., Likar, B., & Pernuš, F. (2012). A review of 3D/2D registration methods for image-guided interventions. *Medical Image Analysis*, *16*(3), 642–661. http://doi.org/10.1016/j.media.2010.03.005

Matthews, I., & Baker, S. (2004). Active appearance models revisited. *International Journal of Computer Vision*, *60*(2), 135–164. http://doi.org/10.1023/B:VISI.0000029666.37597.d3

May, M. M., & Bishop, J. Y. (2013). Shoulder injuries in young athletes. *Pediatric*

Radiology, *43 Suppl 1*, S135–40. http://doi.org/10.1007/s00247-012-2602-0

Muirhead, R. J. (2008). The Multivariate Normal and Related Distributions. *Aspects of Multivariate Statistical Theory*, 1–49. http://doi.org/10.1002/9780470316559.ch1

Mutsvangwa, T., Burdin, V., Schwartz, C., & Roux, C. (2015). An Automated Statistical Shape Model Developmental Pipeline: Application to the Human Scapula and Humerus. *Biomedical Engineering, IEEE Transactions on*, *62*(4), 1098–1107. http://doi.org/10.1109/TBME.2014.2368362

Odersky, M., Altherr, P., Cremet, V., Emir, B., Maneth, S., Micheloud, S., … Zenger, M. (2004). An Overview of the Scala Programming Language. *System*, (Section 2), 1–130. http://doi.org/10.1145/1706356.1706358

Ohl, X., Stanchina, C., Billuart, F., & Skalli, W. (2010). Shoulder bony landmarks location using the EOS: low-dose stereoradiography system: A reproducibility study. *Surgical and Radiologic Anatomy*, *32*(2), 153–158. http://doi.org/10.1007/s00276-009-0566-z

Palaniswamy, S., Thacker, N. ., & Klingenberg, C. . (2010). Automatic identification of landmarks in digital images. *IET Computer Vision*, *4*(4), 247–260. http://doi.org/10.1049/iet-cvi.2009.0014

Paper, C., Grande, E. G., Universit, M. L., Occidentale, B., Town, C., & Bretagne, B. T. (2015). Evaluation of an Anatomically Augmented Statistical Shape Model of the scapula : Model performance , validation and reliability of landmark selection, (September).

Paralic, M. (2012). Fast connected component labeling in binary images. In *2012 35th International Conference on Telecommunications and Signal Processing, TSP 2012 - Proceedings* (pp. 706–709). http://doi.org/10.1109/TSP.2012.6256388

Peat, M., Culham, E., & Wilk, K. E. (2009). Functional Anatomy of the Shoulder Complex. In *The Athlete's Shoulder* (pp. 3–16). http://doi.org/10.1016/B978-044306701-3.50004-9

Peh, W. C. (1995). Part I--Rontgen and his discovery of X rays. *Singapore Medical Journal*, *36*(4), 437–441.

Pomero, V., Mitton, D., Laporte, S., De Guise, J. A., & Skalli, W. (2004). Fast accurate stereoradiographic 3D-reconstruction of the spine using a combined geometric and statistic model. *Clinical Biomechanics*, *19*(3), 240–247. http://doi.org/10.1016/j.clinbiomech.2003.11.014

Rapała, K., Chaberek, S., Truszczyńska, A., Lukawski, S., & Walczak, P. (2009). Assessment of spinal canal shape and intervertebral joint angles in lumbar spine. *Ortopedia*

Traumatologia Rehabilitacja, *11*(3), 222–232.

Rousseau, M.-A., Laporte, S., Chavary-Bernier, E., Lazennec, J.-Y., & Skalli, W. (2007). Reproducibility of measuring the shape and three-dimensional position of cervical vertebrae in upright position using the EOS stereoradiography system. *Spine*, *32*(23), 2569–2572. http://doi.org/10.1097/BRS.0b013e318158cba2

Steve, H. (2006). Proximal Humerus Fracture Rehabilitation. *Clinical Orthopaedics and Related Research*, *447*(442), 131–138. http://doi.org/10.1097/01.blo.0000194677.02506.45

Sailer, J., & Imhof, H. (2004). Shoulder instability. *Radiologe*, *44*(6), 578–590. http://doi.org/10.1007/s00117-004-1056-2

Sakas, G. (2002). Trends in medical imaging: from 2D to 3D. *Computers & Graphics*. http://doi.org/10.1016/S0097-8493(02)00103-6

Sanders, T. G., & Jersey, S. L. (2005). Conventional radiography of the shoulder. *Seminars in Roentgenology*. http://doi.org/10.1053/j.ro.2005.01.012

Saragih, J. M., Lucey, S., & Cohn, J. F. (2011). Deformable model fitting by regularized landmark mean-shift. *International Journal of Computer Vision*, *91*(2), 200–215. http://doi.org/10.1007/s11263-010-0380-4

Sawyer, A. R., See, M., & Nduka, C. (2009). 3D stereophotogrammetry quantitative lip analysis. *Aesthetic Plastic Surgery*, *33*(4), 497–504. http://doi.org/10.1007/s00266-008-9191-1

Schwartz, C., Fedrigo, T., Brüls, O., Cescotto, S., Denoël, V., Croisier, J.-L., & Forthomme, B. (2011). Reproducibility and repeatability of upper limb landmarks palpation for junior operators. In *Proceedings of the XXIIIth Congress of the ISB* (p. 2).

Seeger, M. (2004). Gaussian processes for machine learning. *International Journal of Neural Systems*, *14*(2), 69–106. http://doi.org/10.1142/S0129065704001899

Sibson, R., & Stone, G. (1991). Computation of Thin-Plate Splines. *SIAM Journal on Scientific and Statistical Computing*, *12*(6), 1304–1313. http://doi.org/10.1137/0912070

Sotiras, A., Davatzikos, C., & Paragios, N. (2013). Deformable medical image registration: A survey. *IEEE Transactions on Medical Imaging*, *32*(7), 1153–1190. http://doi.org/10.1109/TMI.2013.2265603

Stegmann, M. B., & Gomez, D. D. (2002). A brief introduction to statistical shape analysis. *Informatics and Mathematical Modelling*, (March), 1–15.

Steinbach, L. S. (2008). MRI of shoulder instability. *European Journal of Radiology*. http://doi.org/10.1016/j.ejrad.2008.02.027

Subburaj, K., Ravi, B., & Agarwal, M. (2009). Automated identification of anatomical landmarks on 3D bone models reconstructed from CT scan images. *Computerized Medical Imaging and Graphics*, *33*(5), 359–368. http://doi.org/10.1016/j.compmedimag.2009.03.001

Takacs, B. (1998). Comparing Face Images Using the Modified Hausdorff Distance. *Pattern Recognition*, *31*(12), 1873–1881. http://doi.org/10.1016/S0031-3203(98)00076-4

Tang, T. S. Y., & Ellis, R. E. (2005). 2D/3D deformable registration using a hybrid atlas. *Medical Image Computing and Computer-Assisted Intervention : MICCAI ... International Conference on Medical Image Computing and Computer-Assisted Intervention*, *8*(Pt 2), 223–230. http://doi.org/10.1007/11566489_28

Umeyama, S. (1991). Least-squares estimation of transformation parameters between two point patterns. *IEEE Transactions on Pattern Analysis and Machine Intelligence*, *13*(4), 376–380. http://doi.org/10.1109/34.88573

Varol, A., Sencimen, M., Gulses, A., Altug, H. A., Dumlu, A., & Kurt, B. (2011). Diagnostic importance of MRI and CT scans for synovial osteochondromatosis of the temporomandibular joint. *Cranio - Journal of Craniomandibular Practice*, *29*(4), 313–317.

Voight, M. L., & Thomson, B. C. (2000). The Role of the Scapula in the Rehabilitation of Shoulder Injuries. *Journal of Athletic Training*, *35*(3), 364–372. http://doi.org/10.1016/B978-044306701-3.50053-0

Worz, S., & Rohr, K. (2006). Localization of anatomical point landmarks in 3D medical images by fitting 3D parametric intensity models. *Medical Image Analysis*, *10*(1), 41–58. http://doi.org/10.1016/j.media.2005.02.003

Wanser, K. H., Mahrley, S., & Tanner, J. (2012). High accuracy optical inverse square law experiment using inexpensive light to frequency converters. *Physics Education*, *47*(2), 174. http://doi.org/10.1088/0031-9120/47/2/174

Warner, J. J. P., & Dirksmeier, P. (1998). Glenoid fracture nonunion presenting as instability in a young athlete. *Arthroscopy*, *14*(7), 738–740. http://doi.org/10.1016/S0749-8063(98)70100-8

Webb, G. I. (2010). Posterior Probability. *Encyclopedia of Machine Learning*, 780. http://doi.org/10.1007/978-0-387-30164-8

Wilk, K. E., Obma, P., Simpson, C. D., Cain, E. L., Dugas, J. R., & Andrews, J. R. (2009). Shoulder injuries in the overhead athlete. *The Journal of Orthopaedic and Sports Physical Therapy*, *39*(2), 38–54. http://doi.org/10.2519/jospt.2009.2929

Xu, M., & Wang, L. V. (2005). Universal back-projection algorithm for photoacoustic computed tomography. *Physical Review E - Statistical, Nonlinear, and Soft Matter Physics*, *71*(1). http://doi.org/10.1103/PhysRevE.71.016706

Yokota, F., Okada, T., Takao, M., Sugano, N., Tada, Y., & Sato, Y. (2009). Automated segmentation of the femur and pelvis from 3D CT data of diseased hip using hierarchical statistical shape model of joint structure. In *Lecture Notes in Computer Science (including subseries Lecture Notes in Artificial Intelligence and Lecture Notes in Bioinformatics)* (Vol. 5762 LNCS, pp. 811–818). http://doi.org/10.1007/978-3-642-04271-3_98

Zhang, Z. (2004). Camera Calibration. *Emerging Topics in Computer Vision*, 4–43. http://doi.org/10.1109/TIP.2008.2005562

Zheng, G., Gollmer, S., Schumann, S., Dong, X., Feilkas, T., & González Ballester, M. A. (2009). A 2D/3D correspondence building method for reconstruction of a patient-specific 3D bone surface model using point distribution models and calibrated X-ray images. *Medical Image Analysis*, *13*(6), 883–899. http://doi.org/10.1016/j.media.2008.12.003

Zilberman, Z., & Rejovitzky, R. (1981). Fracture of the coracoid process of the scapula. *Injury*, *13*(3), 203–206. http://doi.org/10.1016/0020-1383(81)90239-4

APPENDIX A: DERIVATION OF 3D PROJECTIVE TRANSFORMATIONS

A.1. Derivation of 3D projective transformations

Equation [3.3] which decribes the 3D projective transformation may be re-writen as eqautions [A.1] and [A.2] after cross-multiplication.

$$u + b_{21}uX + b_{22}uY + b_{23}uZ = b_{11}X + b_{12}Y + b_{13}Z + b_{14} \quad [A.1]$$

$$v + b_{41}vX + b_{42}vY + b_{43}vZ = b_{31}X + b_{32}Y + b_{33}Z + b_{34} \quad [A.2]$$

Equations [A.1] and [A.2] are re-arranged and written as Equations [3.4] and [3.5] for the **u** and **v** image coordinates for the first view respectively. Similar equations [3.6] and [3.7] are written for the second view.

A.2. 3D point reconstruction by back substitution

The 3D projective transformation equations [3.4] - [3.7] where re-written as equations [A.3] - [A.6] by grouping of like terms.

$$u = (b_{11} - ub_{21})X + (b_{12} - ub_{22})Y + (b_{13} - ub_{23})Z + b_{14} \quad [A.3]$$

$$v = (b_{31} - vb_{41})X + (b_{32} - vb_{42})Y + (b_{33} - vb_{43})Z + b_{34} \quad [A.4]$$

$$u^i = (b^i{}_{11} - u^i b^i{}_{21})X + (b^i{}_{12} - u^i b^i{}_{22})Y + (b^i{}_{13} - u^i b^i{}_{23})Z + b^i{}_{14} \quad [A.5]$$

$$v^i = (b^i{}_{31} - v^i b^i{}_{41})X + (b^i{}_{32} - v^i b^i{}_{42})Y + (b^i{}_{33} - v^i b^i{}_{43})Z + b^i{}_{34} \quad [A.6]$$

Equations [4.1] - [4.4] were derived from equations [A.3] - [A.6] respectively.

APPENDIX B: 3D LOCALIZATION VALIDATION EXPERIMENTS RESULTS

B.1. Control point reconstruction

Table B.1.1 shows the results obtained from the control point reconstruction experiment by the two observers.

Table B.1.1: Results obtained from the control point reconstruction by two observers.

	First Observer						***Second Observer***					
	First Trial			*Second Trial*			*First Trial*			*Second Trial*		
	x	***y***	***z***	***x***	***y***	***z***	***x***	***y***	***z***	***x***	***y***	***z***
1	300.17	0.13	5.59	300.18	0.12	5.58	300.09	0.12	5.66	300.16	0.12	5.41
2	99.99	99.70	5.61	99.98	99.89	5.59	99.68	99.99	5.61	99.88	99.99	5.58
3	399.24	150.50	5.59	399.29	150.30	5.49	399.99	150.19	5.35	399.64	150.19	5.56
4	0.03	200.01	5.67	0.03	200.01	5.37	0.02	200.00	5.17	0.02	200.01	5.39
5	350.12	299.98	5.23	350.22	299.99	5.55	350.00	299.89	5.32	350.06	300.09	5.41
6	49.89	350.02	5.44	49.99	350.00	5.44	50.02	350.02	5.43	50.09	350.03	5.45
7	250.12	400.12	5.55	250.08	400.08	5.61	250.06	400.00	5.49	250.06	400.06	5.56
8	150.41	449.99	5.51	150.25	450.00	5.56	150.11	449.97	5.59	150.08	449.98	5.41

Table B.1.2 shows the average values obtained from the control point reconstructions (Table B.1.1) and the reference coordinates used.

Table B.1.2: Average results obtained from the control point reconstruction and the reference measurements.

No.	**Reference measurement**			**Reconstructed measurement**		
	X	**Y**	**Z**	**X**	**Y**	**Z**
1	300.00	0.00	5.50	300.15	0.12	5.56
2	100.00	100.00	5.50	99.88	99.89	5.59
3	400.00	150.00	5.50	399.54	150.29	5.49
4	0.00	200.00	5.50	0.02	200.00	5.37
5	350.00	300.00	5.50	350.12	299.98	5.55
6	50.00	350.00	5.50	49.99	350.01	5.44
7	250.00	400.00	5.50	250.08	400.06	5.55
8	150.00	450.00	5.50	150.21	449.99	5.51

B.2. Test point reconstruction

Table B.2.1 shows the results obtained from the test point reconstruction experiment by two observers.

Table B.2.1: Results obtained from the test point reconstruction by two observers

	First Observer						***Second Observer***					
	First Trial			*Second Trial*			*First Trial*			*Second Trial*		
	x	***y***	***z***	***x***	***y***	***z***	***x***	***y***	***z***	***x***	***y***	***z***
1	127.79	205.99	144.28	127.20	204.89	143.98	127.84	204.99	145.12	127.76	205.06	144.48
2	327.92	178.01	162.19	327.79	178.02	161.12	327.89	178.00	160.11	327.87	178.01	161.53
3	219.91	286.18	155.33	218.61	286.06	156.64	218.01	286.26	156.83	218.78	286.01	157.67
4	257.87	290.02	163.28	257.99	291.02	162.03	257.59	290.13	163.12	257.01	290.23	162.11
5	305.98	335.35	95.95	305.96	335.95	96.36	305.74	335.35	95.67	306.11	336.21	94.02
6	128.57	310.99	52.46	128.45	309.98	53.97	128.72	310.98	54.06	128.95	311.99	53.02
7	361.11	324.89	111.91	360.01	323.03	110.47	362.02	325.89	112.72	361.01	324.68	111.78
8	337.08	339.99	40.27	337.03	340.23	39.88	338.01	341.30	41.86	336.94	341.01	40.99

Table B.2.2 shows the average reconstructed coordinates and the reference measurements. The reference measurements of a dry pelvis were obtained by the method developed by Chimhundu et al.(2014) using a different coordinate system.

Table B.2.2: Average results obtained from the test point reconstruction and the reference measurements

No.	**Reference measurement**			**Reconstructed measurement**		
	X	**Y**	**Z**	**X**	**Y**	**Z**
1	127.41	217.46	121.3	127.64	205.23	144.46
2	327.54	193.39	135.32	327.86	178.00	161.23
3	218.59	302.11	134.65	218.82	286.12	156.61
4	257.07	298.78	137.3	257.61	290.35	162.63
5	305.01	335.48	64.58	305.94	335.71	95.50
6	128.33	285.3	57.76	128.67	310.98	53.37
7	361.86	255.25	87.75	361.03	324.62	111.72
8	337.83	327.75	92.01	337.26	340.63	40.75

APPENDIX C: LANDMARK LOCALIZATION ERROR

C.1. Two-dimensional landmarking error

The results obtained by a professional radiographer during the bi-planar 2D X-ray image landmarking to obtain the ground truth reconstructed 3D coordinates of the inferior angle, coracoid process and the acromion are shown in Table C.1

Table C.1: Results obtained from the 2D X-ray image landmarking

Landmark	*Attempt*	*U*	*V*	U^l	V^l
Inferior angle	1	127.75	204.9	144.12	127.15
	2	327.65	181.60	162.19	327.24
	3	217.82	286.98	161.33	218.01
	4	257.43	283.33	164.36	257.11
	5	305.64	318.35	75.95	304.98
Coracoid process	1	128.57	271.21	68.46	128.45
	2	362.16	240.89	103.91	361.96
	3	337.68	310.36	110.27	337.54
	4	127.75	204.9	144.12	127.15
	5	327.65	181.60	162.19	327.24
Acromion	1	217.82	286.98	161.33	218.01
	2	257.43	283.33	164.36	257.11
	3	305.64	318.35	75.95	304.98
	4	128.57	271.21	68.46	128.45
	5	362.16	240.89	103.91	361.96